Triple junction benchmark for multiphase-field and multi-order parameter models

Simon Daubner[a], Paul W. Hoffrogge[a], Martin Minar[c], Britta Nestler[a,b]

[a]*Institute for Applied Materials (IAM-MMS), Karlsruhe Institute of Technology, Strasse am Forum 7, 76131, Karlsruhe, Germany*
[b]*Institute for Digital Materials Science (IDM), Karlsruhe University of Applied Sciences, Moltkestrasse 30, 76133 Karlsruhe, Germany*
[c]*Department of Materials Engineering, KU Leuven, Kasteelpark Arenberg 44, 3001 Leuven, Belgium*

Abstract

Due to their ability to encompass complex multi-phase problems, multiphase-field and multi-order parameter methods are increasing in popularity. Multiple model formulations and modifications have been published since their original emergence but a comprehensive comparison has not yet been conducted. We establish the triple junction as a well-defined benchmark for the construction of interfacial energy contributions. Metrics such as the overall free energy of the system and the dihedral angle at the junction are derived from analytic considerations and subsequently evaluated in numerical studies. Various multiphase-field and multi-order parameter models are compared quantitatively over a large range of interfacial energy ratios. The analytic derivations for the two benchmark cases form a strong foundation for identification of model-specific errors or a limited application range. The mutual comparison of combinations of various gradient and potential energy terms yields new insights into the sources of spurious phase generation. The systematic combination of terms covers previously published models as well as new combinations. This work provides guidelines for the choice of a suitable, problem-specific model formulation and the development of new models. Furthermore, our goal is to be as comprehensible as possible to ensure high reproducibility and facilitate the start for beginners in the field.

Keywords: phase-field method, benchmark, triple junction, multiphase-field models, multi-order parameter models

1. Introduction

Over the last decades, phase-field methods have been established as the method of choice for the simulation of microstructures with evolving interfaces. A general feature of phase-field approaches is the diffuse interface between coexisting phases. The term phase refers to thermodynamically distinct states that occur in a phase diagram as a function of temperature, pressure, composition, and so on. In the phase-field community, the usage of this term extends to differentiate between crystalline polymorphs or grains with different orientations but equal chemical properties. The diffuse interface is characterized by a continuous and steep transition of the phase-field variable, which generally could be molar fraction c [1], an order parameter η [2–4] or the volume fraction ϕ [5, 6] of the respective phase. In many fundamental works of the phase-field method [1, 7, 8], the diffusiveness of interfaces is considered a natural property of the transition region between stable phases which holds true on a small scale. In many applications, the phase-field method is primarily used due to its strength to describe curved and evolving surfaces but the physical length scale of the diffuse interface is well below the microstructural scale of interest. This introduces the

notion of diffuse representation of sharp-interface problems which calls for effective re-scaling of the diffuse interfacial width while preserving its physical interfacial energy to correctly model the interplay of curvature driven phase transformations with other coupled multi-physics. Applications of the phase-field method range from solidification such as dendritic growth [9] or lamellae for eutectic systems [6, 10, 11] to fields such as microstructure evolution in fuel cells [12] or intercalation in battery materials [13, 14]. For all these applications, the simulation outcome heavily depends on the correct modeling of competing driving forces and, irrespective of the possibly coupled multiphysics, always depends on interfacial energies and, thus, curvature driving forces.

In multiphase systems, interfaces intersect at common points, so-called junctions, where the balance of interfacial tensions is fulfilled in equilibrium. In the non-equilibrium case, the deviation from equilibrium may be quantified by incorporating finite triple-junction mobilities [15, p. 379] . Given the fact that no model takes this effect explicitly into account, any deviation from the force balance is a model artifact. The balance of interfacial tensions is not explicitly imposed in multiphase-field models, but rather subtly introduced by construction of a suitable functional. Some multi-phase extensions of interfacial energies lead to spurious phases (also called ghost phases) which distort the force balance in junctions of polycrystalline systems.

Generalizations of the phase-field method to multi-phase systems were developed in two different ways, both acting as a nucleus for the growth of scientific communities. In 1994, Chen and Yang [3] published a model employing many nonconserved order parameters evolving through time-dependent Ginzburg-Landau equations and started the model branch of **multi-order parameter models** (also called continuum-field models). The work by Steinbach *et al.* [5] in 1996 marks the beginning of **multiphase-field models** which are characterized by the notion of phase-fields ϕ representing the volume fraction. Both branches have been further developed since. As a result, many model formulations are based on the same principles but differ in details. For instance, various formulations of the potential energy term (also called barrier energy or homogeneous term) can be found in current literature [6, 16–18]. Many published models have been validated computationally using Young's law for triple junctions or employing mathematical techniques to compare with sharp interface solutions. Asymptotic analysis is a powerful tool which has been used to show the match with analytic predictions in the sharp-interface limit. However, this method has mainly been applied to two-phase interfaces. Very few authors check the validity of Young's law analytically [19, 20]. The occurance of spurious phases is still a common problem in practical simulations with finite interface width as they alter the energy of the system and, thus, distort equilibrium angles in higher-order junctions. Even though there are ways to avoid them, implications of the different approaches for the model behavior were not investigated extensively in the past. Furthermore, some works modify the evolution equations of phases (e.g. by neglecting cross-terms [5, 21, 22]) to reduce computational cost, often without quantifying the possible error or stating the limits of this assumption. Last but not least, multi-phase field formulations have historically been developed by various research groups, each of them following their own notation and advancing their own branch of model development. There has been little effort to address the mutual comparison of phase-field formulations. The work by Moelans, Wendler and Nestler [23] compares two phase-field models, employing a steady-state triple junction amongst others but is limited to dihedral angles in the range $\theta \in [89, 140]$. Toth *et al.* [18] were the first, to the best of our knowledge, to define a list of criteria that should be fulfilled for any multiphase-field formulation. Using these criteria, the authors compare established models with a newly developed one. For the scope of this work, we employ some of the criteria and only consider model formulations which fulfill the following conditions [18]:

- In accordance with the "principle of formal indistinguishability", physical results should be independent of the labeling of variables (i.e. independent of the order of computation).

- Over time, the total free energy should decrease monotonically (second law of thermodynamics) and tend towards the equilibrium solution which minimizes the free energy of the system.

- The model should be general in the sense that adding or removing a new phase is straight-forward and it should be possible to recover the respective models from each other, e.g. all formulations naturally reduce to the well-known equations of a two-phase interface for $N = 2$.

Other criteria from [18] will be evaluated in Sec. 4. The goal of this work is to shed some light on the similarities and differences among various branches of multi-phase field (MPF) as well as multi-order parameter (MOP) models, performed in three consecutive steps. In Sec. 2, commonly used gradient and potential energy contributions for both MPF as well as MOP models are compared using a unified notation. Subsequently, we elaborate on the differences between the two families of models by specifying evolution equations, underlying assumptions as well as the inclusion of physical model parameters separately for MOP (Sec. 2.3) and MPF models (Sec. 2.4). We then establish the triple junction as a benchmark case for MPF and MOP models starting from sharp interface analytics for a static and steady-state case in Sec. 3. Multiple authors have previously used a triple junction setup to validate their specific modeling approach [17, 20, 23–26] which is well-suited for the following reasons:

- All critical modeling choices for extension from the two-phase to the multi-phase case have to be made to arrive at a triple junction. It should then be straight-forward to increase the number of phases to N.

- The energetic landscape of the potential term can still be visualized employing the Gibbs simplex constraint, similar to a ternary diagram (see [25] and Sec. 2.2).

- Triple junction angles are analytically known from Young's law.

- The occurance of ghost phases can be quantified.

- The simulation setup is simple enough (concerning initial and boundary conditions, domain size, computational effort) to be suitable for benchmarking.

The steady-state motion of the triple junction has often been compared with an analytical solution derived from a small-slope approximation [23, 27] without discussing the limits of this approximation. Especially at high ratios of the pair-wise interfacial energies, the approximate solution deviates strongly from the mathematically exact solution [15, 28] which impacts the drawn conclusions. This issue has been addressed in a recent note by Eiken [29]. Sec. 4 is dedicated to the quantitative comparison of various modeling approaches using well-defined metrics such as total energy of the system and the dihedral angle at the triple junction. Finally, we conclude this work in Sec. 5 and hope to provide guidelines for users of the phase-field method by discussing the subtle differences between the formulations.

2. Model formulation

Multiphase-field models are formulated in terms of a tuple of N phase variables $\boldsymbol{\phi} = \{\phi_\alpha, \phi_\beta, \dots\}$ where ϕ_α denotes the volume fraction of the α-phase and thus $\phi_\alpha \in [0, 1]$ and $\sum_\alpha^N \phi_\alpha = 1$ should be fulfilled [6, 16, 30, 31]. Multi-order parameter models, on the other hand, employ a tuple of order parameters $\boldsymbol{\eta} = \{\eta_\alpha, \eta_\beta, \dots\}$ that indicate the respective phase but have no direct physical interpretation [2, 4]. Nevertheless, in these models the energy landscape is designed in such a way that local minima promote stable states which can each be mapped to a certain phase. Thus, the bulk of phase α is usually identified as the region where the value of η_α is close, but not necessarily equal, to the location of the respective minimum. Depending on the energy formulation, stable states of η can e.g. be $-\eta_0, 0, \eta_0$ where η_0 depends on the energy fitting parameters [32] or $0, 1$ [33]. Due to the large variety of notation conventions used among the phase-field community, it is difficult to grasp differences among the various model formulations. Often, the same symbols denote substantially different parameters and even some terms can have divergent meanings (e.g. the term obstacle potential barrier denotes a different parameter in MPF as in MOP models). For this reason, Table C.6 gives an overview of various notations used in selected original publications while the model formulation within this work aims at unifying the various notations. For the formulation of the energy functional and possible choices of energy contributions, we restrict ourselves to formulations with stable states 0 and 1. We use the symbol η for the formulation of MOP evolution equations in Sec. 2.3 and ϕ for MPF models in Sec. 2.4 to differentiate between the aforementioned physical interpretations. In terms of computation, this is reflected by the fact that the Gibbs simplex constraint (see Appendix D) needs to

be explicitly enforced in MPF models. The free energy contributions in Sec. 2.1 and 2.2 are formulated in terms of ϕ which is an arbitrary choice.

In a general sense, the energy functional can be formulated as

$$\mathcal{F}(\phi, \nabla\phi, \dots) = \mathcal{F}_{\text{int}}(\phi, \nabla\phi) + \mathcal{F}_{\text{bulk}}(\phi, \dots) \tag{1}$$

where we assume a separation of interfacial and bulk energy terms following the notion discussed in the introduction that sharp interfaces can be replaced by a diffuse representation well above the atomic scale of diffuse transition regions. The interfacial term represents the surface energy of phases in contact with each other. In a sharp interface representation, this energy contribution is constrained to surfaces but in the context of the phase-field approach, it turns into a volumetric contribution smeared over the diffuse interface region such that $\mathcal{F}_{\text{int}} = \int_V f_{\text{int}} \mathrm{d}V$ holds. The integral should converge to the same energy even for finite interfacial widths. The bulk contribution can possibly contain chemical, mechanical, thermal, electrical or other driving forces for phase transformation but is not subject of the following investigations. The interfacial volume integral of phase-field formulations is generally constructed as the sum over two contributions

$$\mathcal{F}_{\text{int}}(\phi, \nabla\phi) = \int_V f_{\text{grad}}(\phi, \nabla\phi) + f_{\text{pot}}(\phi) \mathrm{d}V \tag{2}$$

namely a gradient term and a potential term (also called homogeneous free energy [17] or barrier function [18]) which will be discussed in detail in the following sections.

2.1. Gradient energy formulations

As a generalization of the two-phase case $\kappa|\nabla\phi|^2$, we formulate the gradient term for multiple phases $\alpha, \beta, \dots N$ as

$$f_{\text{grad}}(\nabla\phi) = \frac{1}{2}\sum_\alpha\sum_\beta(\nabla\phi_\alpha : \kappa_{\alpha\beta} : \nabla\phi_\beta) \stackrel{\text{isotropic}}{=} \frac{1}{2}\sum_\alpha\sum_\beta \kappa_{\alpha\beta}(\nabla\phi_\alpha \cdot \nabla\phi_\beta) \tag{3}$$

where $\kappa_{\alpha\beta}$ could be a tensor including directional dependence of interfacial energies. For isotropic systems, it reduces to a scalar $\kappa_{\alpha\beta}$. Note that there are various other ways to include anisotropic surface energies within phase-field formulations [18, 34]. Some model formulations only employ the main diagonal of the $\kappa_{\alpha\beta}$-matrix, i.e. $\kappa_{\alpha\beta} = 0, \forall \alpha \neq \beta$ which results in

$$f_{\text{grad}}(\nabla\phi) = \frac{1}{2}\sum_\alpha \kappa_\alpha|\nabla\phi_\alpha|^2. \tag{4}$$

This formulation carries the problem that for a number of phases $N > 3$ there are less parameters κ_α than possibly different pairwise interfacial energies $\gamma_{\alpha\beta}$ which leads to the alternative formulation based on interpolation of the pairwise parameters $\kappa_{\alpha\beta}$

$$f_{\text{grad}}^{\text{interpolate}}(\phi, \nabla\phi) = \frac{\tilde{\kappa}}{2}\sum_\alpha |\nabla\phi_\alpha|^2 \quad \text{where } \tilde{\kappa} = \frac{\sum \kappa_{\alpha\beta} h_{\alpha\beta}(\phi)}{\sum h_{\alpha\beta}(\phi)}. \tag{5}$$

A popular choice is $h_{\alpha\beta} = \phi_\alpha^2\phi_\beta^2$ [17, 18, 33], but generally the definition of an appropriate interpolation function can be challenging. Due to the interpolation, this formulation is not only a function of gradients $\nabla\phi_\alpha$ but also the ϕ_α-values. Alternatively, setting the main diagonal to zero $\kappa_{\alpha\alpha} = 0$ leads to a second set of frequently used gradient formulations [16]. As the interfacial energy $\gamma_{\alpha\beta}$ between two phases should be independent of the labeling of variables (see principle of formal indistinguishability [18]), we enforce symmetry $\kappa_{\alpha\beta} = \kappa_{\beta\alpha}$. The gradient term can thus be written as the summation over pairwise dot products

$$f_{\text{grad}}^{\text{dot}}(\nabla\phi) = -\sum_\alpha\sum_{\beta>\alpha} \kappa_{\alpha\beta}\nabla\phi_\alpha \cdot \nabla\phi_\beta \tag{6}$$

4

where the minus sign is introduced for convenience of the $\kappa_{\alpha\beta}$ fitting values. Note that the factor $1/2$ is consumed by assumption of symmetry and reduction to the upper right entries of the matrix $(\sum_{\beta > \alpha})$. Another formulation of the gradient term which has been used in works of Steinbach [5], Tiaden [35] and Nestler [6, 36]

$$f_{\text{grad}}^{\text{weighted}}(\boldsymbol{\phi}, \boldsymbol{\nabla}\boldsymbol{\phi}) = \sum_{\alpha} \sum_{\beta > \alpha} \kappa_{\alpha\beta} |\phi_\alpha \boldsymbol{\nabla}\phi_\beta - \phi_\beta \boldsymbol{\nabla}\phi_\alpha|^2 \tag{7}$$

cannot be derived from the postulated Eq. (3) but is closely related to formulation Eq. (6) in the sense that terms are introduced as pairwise interactions with parameters $\kappa_{\alpha\beta}$. It includes a generalized gradient based on an antisymmetric weighting of the two gradients for each two-phase interface and traces back to the theory of irreducible representation (see Landau and Lifschitz [37]). An important feature that both equations 6 and 7 share is that the $\alpha\beta$ term vanishes in all other interfaces where one of the two phases is inactive ($\phi_\alpha = 0$ and $\boldsymbol{\nabla}\phi_\alpha = 0$ or $\phi_\beta = 0$ and $\boldsymbol{\nabla}\phi_\beta = 0$). This ensures that the interfacial energies are mutually decoupled, which simplifies the parameterization of the model. All the above mentioned formulations reduce to $\kappa|\boldsymbol{\nabla}\phi_\alpha|^2$ in two-phase interfaces if $\phi_\beta = 1 - \phi_\alpha$ (which implies $\boldsymbol{\nabla}\phi_\beta = -\boldsymbol{\nabla}\phi_\alpha$) is fulfilled.

2.2. Potential energy formulations

The double-well and double-obstacle formulations which have typically been used for phase-field models with one parameter $f_{\text{well}}(\phi) = \Omega\phi^2(1 - \phi)^2$ and $f_{\text{ob}}(\phi) = \Omega\phi(1 - \phi)$ (see Appendix A) can be generalized intuitively in two possible ways. The first one is motivated by setting $\phi = \phi_\alpha$ and defining the second phase as $\phi_\beta = 1 - \phi$ which results in

$$f_{\text{well}}^1(\boldsymbol{\phi}) = \sum_{\alpha} \sum_{\beta > \alpha} \Omega_{\alpha\beta} \phi_\alpha^2 \phi_\beta^2 \quad \text{and} \quad f_{\text{ob}}^1(\boldsymbol{\phi}) = \sum_{\alpha} \sum_{\beta > \alpha} \Omega_{\alpha\beta} \phi_\alpha \phi_\beta.$$

The second option is a summation over all occurring phases where we set $\phi = \phi_\alpha$ in the single phase terms

$$f_{\text{well}}^2(\boldsymbol{\phi}) = \frac{1}{2} \sum_{\alpha} \Omega_\alpha \phi_\alpha^2 (1 - \phi_\alpha)^2 \quad \text{and} \quad f_{\text{ob}}^2(\boldsymbol{\phi}) = \frac{1}{2} \sum_{\alpha} \Omega_\alpha \phi_\alpha (1 - \phi_\alpha).$$

Other formulations are generally possible under the constraint that they naturally reduce to the double-well or obstacle potential within each two-phase interface to reproduce the physical interfacial energy $\gamma_{\alpha\beta}$ of each $\alpha\beta$-phase pair. This implicitly requires the additional criterion that two-phase interfaces should represent a stable equilibrium and thus be free of additional phases [18]. The occurrence of additional phases is often referred to as "spurious phases" or "ghost phases" as they are unphysical and alter the resulting interfacial energy. For a more detailed investigation of the above free energy formulations, a three-phase system is considered in the following paragraph.

As mentioned by Folch and Plapp [25], the visualization of the energy landscape over the Gibbs simplex of a triple junction (similar to a ternary diagram) is helpful to aquire geometric intuition. As we make use of the sum constraint $\sum \phi_\alpha = 1$ for parametrization, the energies shown in Fig. 1 are exact for multiphase-field models while differences can arise for multi-order parameter models. However, as the models discussed in this paper assume stable states of η at 0 and 1, most conclusions hold true for both classes of model formulations. By plotting the above formulations with the same value of Ω for all phases (or phase pairs), we can immediately see that the first generalization of the multi-well potential exhibits a saddle at the triple point $\phi_\alpha = \phi_\beta = \phi_\gamma = 1/3$ while for the second approach, the energy of dual interphases is lower than anywhere in the triple phase region. For the obstacle potential, both formulations yield identical results and the energies of two-phase interfaces are generally lower than triple junctions. Differences will be discussed in more detail within the following subsections.

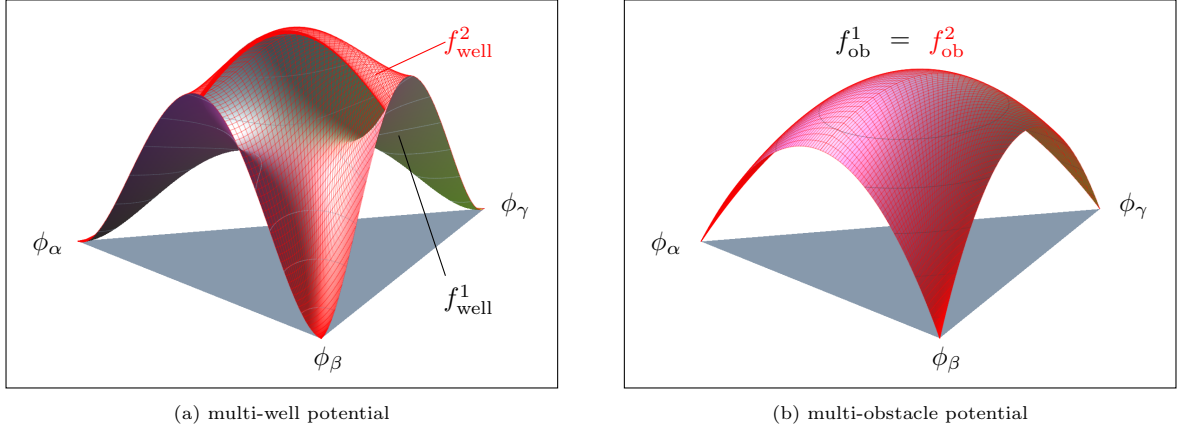(a) multi-well potential   (b) multi-obstacle potential

Figure 1: Energetic landscape of the multi-well and multi-obstacle potentials shown for a three-phase system over the Gibbs simplex of a triple junction. Formulations f_{well}^1 and f_{ob}^1 are represented by surfaces with contour lines while f_{well}^2 and f_{ob}^2 are drawn by red wireframe plots.

2.2.1. Multi-well energies

Throughout the phase-field community, several multi-phase extensions of the well-potential have been applied. Folch and Plapp [25] use formulation $f_{\text{well}}^2(\boldsymbol{\phi})$ for a ternary system. From Fig 1a, it is clear that formulation f_{well}^1, which is purely based on $\phi_\alpha^2\phi_\beta^2$ terms, suffers from low energy in the triple junction. As the three-phase case becomes energetically favorable compared to two-phase interfaces, models based on this approach suffer from ghost phases and distorted interfacial energies. Some multi-well formulations try to circumvent this issue by adding additional terms that penalize higher-order junctions through single phase contributions that need to be constructed such that they reduce correctly in the two-phase case

$$\text{Moelans } et\ al.[17]\quad f_{\text{well}}^{\text{Moelans}} = \tilde{\Omega}\left(\sum_\alpha \sum_{\beta>\alpha} \chi_{\alpha\beta}\phi_\alpha^2\phi_\beta^2 + \sum_\alpha\left(\frac{\phi_\alpha^4}{4} - \frac{\phi_\alpha^2}{2}\right) + \frac{1}{4}\right) \tag{8}$$

$$\text{Toth } et\ al.[18]\quad f_{\text{well}}^{\text{Toth}} = \tilde{\Omega}\left(\frac{1}{2}\sum_\alpha \sum_{\beta>\alpha} \phi_\alpha^2\phi_\beta^2 + \sum_\alpha\left(\frac{\phi_\alpha^4}{4} - \frac{\phi_\alpha^3}{3}\right) + \frac{1}{12}\right). \tag{9}$$

Alternatively, triple-phase terms can be added

$$\text{Garcke } et\ al.\ [24]\quad f_{\text{well}}^{\text{Garcke}} = \sum_\alpha \sum_{\beta>\alpha} \Omega_{\alpha\beta}\phi_\alpha^2\phi_\beta^2 + \sum_\alpha \sum_{\beta>\alpha} \sum_{\gamma>\beta} \Omega_{\alpha\beta\gamma}\phi_\alpha^2\phi_\beta^2\phi_\gamma^2 \tag{10}$$

to alter the triple junction energy. Other higher-order monomials have been used in works of Steinbach et $al.$ [5] and Tiaden et $al.$ [35]. The similarity between the potentials (9) and (8) is most apparent when both are written for a homogeneous system (as in ideal grain growth)

$$f_{\text{well}}^{\text{Moelans}} = \Omega\left(\chi^{\text{M}}\sum_\alpha \sum_{\beta>\alpha} \phi_\alpha^2\phi_\beta^2 + \sum_\alpha\left(\frac{\phi_\alpha^4}{4} - \frac{\phi_\alpha^2}{2}\right) + \frac{1}{4}\right) \tag{11}$$

$$f_{\text{well}}^{\text{Toth}} = \Omega\left(\chi^{\text{T}}\sum_\alpha \sum_{\beta>\alpha} \phi_\alpha^2\phi_\beta^2 + \sum_\alpha\left(\frac{\phi_\alpha^4}{4} - \frac{\phi_\alpha^3}{3}\right) + \frac{1}{12}\right). \tag{12}$$

The formulations only differ in the polynomial contributions, but interestingly, they reduce to the same expression in the two-phase interface such that the condition $\Omega(2\chi + 1) = 2\Omega_{\text{ref}}$ should be fulfilled (see Appendix A and Appendix B). The parameter χ performs a weighting between the dual terms and single-phase
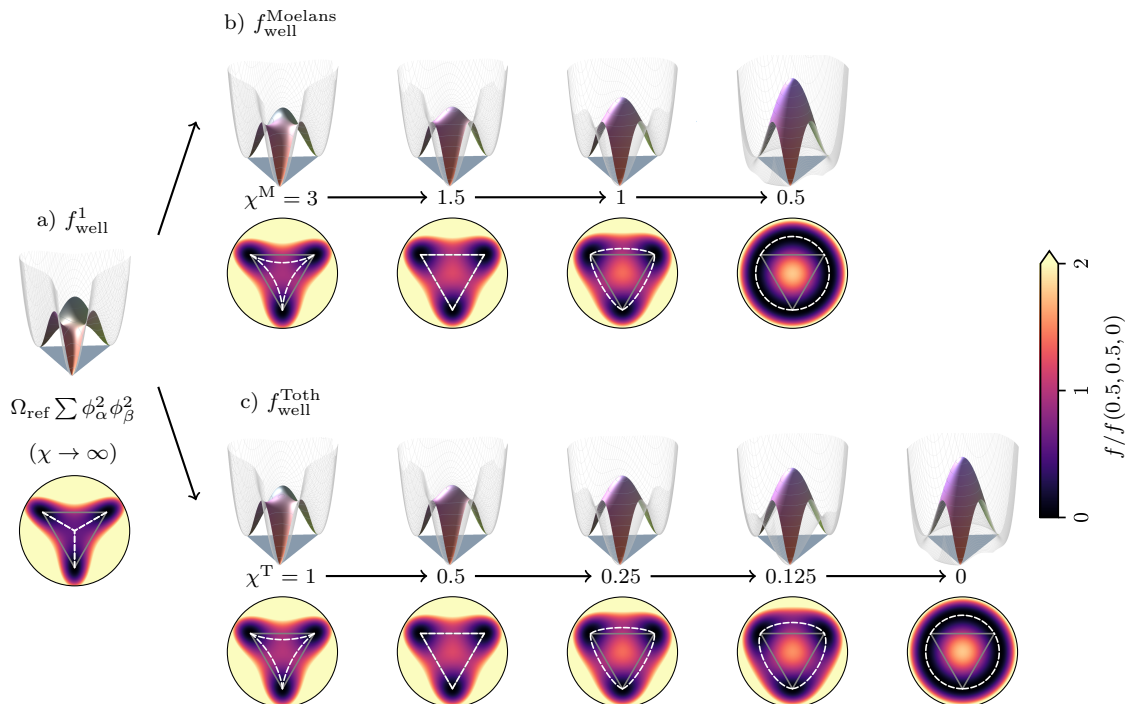
6

Figure 2: Multi-well formulations (11) and (12) drawn over the Gibbs simplex of a triple junction for different values of χ. Energy values inside the sum constraint are shown as colored surfaces with contour lines while values outside are shown by gray wireframe plots. The 2D-colorplots additionally show the minimum-energy path (MEP) between the bulk phases as a white dashed line. The MEP is calculated numerically using the nudged elastic band method [38, 39].

monomials. Fig. 2 shows the energetic landscape over the triple junction for both formulations with constant Ω_{ref} but varying values of χ.

To predict the energy barrier and phase fractions in an interface between two phases, we compute the connecting minimum energy path (MEP) between global minima via the nudged elastic band method [38, 39]. Results are shown in Fig. 2 as white dashed lines in the two-dimensional colorplots. Only for the special values of $\chi^{\mathrm{M}} = 1.5$ and $\chi^{\mathrm{T}} = 0.5$, the behavior of a two-phase system is reproduced. For other values of χ, we expect ghost phases as the minimum energy path involves nonzero values of a third phase. The illustration underlines that not only the values of the potential function within the Gibbs simplex constraint are relevant but also the position of the saddle point which defines the energetic barrier. The saddle point that separates α and β phases is located at $\phi_\alpha = \phi_\beta = (1 - x)/2$ and $\phi_\gamma = x$, where x depends on the value of χ. In the limit of $\chi \to \infty$, both model formulations reduce to the binary terms in f_{well}^1 and the saddle is located at $[1/3, 1/3, 1/3]$. Decreasing the value of χ leads to higher triple point energies until, eventually, two-phase interfaces become energetically favorable and thus a stable solution of the system. The two energy landscapes are identical with formulation f_{well}^2 for the values $\chi^{\mathrm{M}} = 1.5$ and $\chi^{\mathrm{T}} = 0.5$. The saddle point lies on the two-phase interface at $[1/2, 1/2, 0]$ which makes these cases attractive in the sense that they are naturally bounded to the Gibbs simplex and make projection algorithms as discussed in Appendix D redundant. Formulation (11) has an infinite amount of stable solutions that lie on a circle around the Gibbs triangle for $\chi = 0.5$ [4] and, thus, is limited to $\chi \geq 0.5$. The formulation $f_{\mathrm{well}}^{\mathrm{Toth}}$ only reaches this limiting case asymptotically for $\chi \to 0$ which allows a wider range of input parameters. Note that for values smaller than 0.5, the saddle point is located at $x < 0$ which lowers the simulated interfacial energy for multi-order parameter models and, in the case of multi-phase field models, needs explicit handling of the Gibbs simplex constraint.

Hence, it seems beneficial to limit the value χ to a small range of values around 1.5 for Eq. (11) and

0.5 for Eq. (12), respectively, to reach the desired features of multi-well formulations. Moelans *et al.* studied the influence of χ^{M} (there called *overlap parameter*) on the shape of equilibrium phase field profiles and the interfacial energy in two-phase interfaces in more detail in the context of MOP models [17]. If interfacial energies are pair-wise different, this inhomogeneity can be introduced in Eqs. (11) and (12) either via the potential barrier height $\tilde{\Omega} = (\sum \Omega_{\alpha\beta} \phi_\alpha^2 \phi_\beta^2)/(\sum \phi_\alpha^2 \phi_\beta^2)$ or via the weighting parameter $\tilde{\chi} = (\sum \chi_{\alpha\beta} \phi_\alpha^2 \phi_\beta^2)/(\sum \phi_\alpha^2 \phi_\beta^2)$. Implications of these two choices are discussed in [17] and studied in detail in the simulation section 4.

The third formulation Eq. (10) raises the energy in the triple junction, but only in the limit of $\Omega_{\alpha\beta\gamma} \to \infty$ are two-phase interfaces energetically favorable. For finite values of $\Omega_{\alpha\beta\gamma}$, a small fraction of ghost phases remains as can be observed from the simulations in Sec. 4. An additional problem with the triplet terms $\Omega_{\alpha\beta\gamma} \phi_\alpha^2 \phi_\beta^2 \phi_\gamma^2$ is the great number of numerical fitting parameters that results from many phase variables N as it scales with $\propto N^3$. Furthermore, these numerical parameters might cause issues in applications that employ heterogeneous nucleation mechanisms (e.g. martensitic transformations [40] or battery materials [41]) as they crucially influence the nucleation barriers of new phases within existing interfaces.

2.2.2. Multi-obstacle energies

In the case of the obstacle potential, both generalizations shown in Fig. 1b are identical which traces back to the re-formulation

$$\frac{1}{2} \sum_\alpha \Omega \phi_\alpha (1 - \phi_\alpha) = \frac{1}{2} \sum_\alpha \Omega \phi_\alpha \sum_{\beta \neq \alpha} \phi_\beta = \Omega \sum_\alpha \sum_{\beta > \alpha} \phi_\alpha \phi_\beta.$$

This generally holds as long as Ω is identical for all phase-pairs. Formulation f_{ob}^2 suffers from the problem that there are less parameters Ω_α than possible phase-pairs for $N > 3$ which is why we restrict all following simulation examples including the obstacle potential to

$$f_{\mathrm{ob}}(\boldsymbol{\phi}) = \sum_\alpha \sum_{\beta > \alpha} \Omega_{\alpha\beta} \phi_\alpha \phi_\beta \tag{13}$$

which has been extensively used in works from the groups of Steinbach [16] and Nestler [6].

2.3. Multi-order parameter evolution equations

Within the MOP approach, the kinetics of phase transformations are described by the evolution of a tuple of non-conserved order parameters $\boldsymbol{\eta} = \{\eta_\alpha, \eta_\beta, \dots\}$. These fields do not have a direct physical interpretation, although the volume fractions of individual entities can be calculated using interpolation functions [33]. Following the Hamilton's principle, the equilibrium solution is given by $\delta\mathcal{F} = 0$ and we assume linear relaxation of the system free energy towards its minimum. The evolution of order parameters η_α is then governed by

$$\frac{\partial \eta_\alpha}{\partial t} = -L \left(\frac{\partial f}{\partial \eta_\alpha} - \boldsymbol{\nabla} \cdot \frac{\partial f}{\partial \boldsymbol{\nabla} \eta_\alpha} \right) \tag{14}$$

where f denotes the total energy density given by $f = f_{\mathrm{grad}} + f_{\mathrm{pot}}$ in this case. L denotes the kinetic coefficient. As discussed before, the energy terms need to be constructed such that stable equilibria can be associated with the bulk of a phase which excludes the obstacle potential (Eq. (13)) as a potential candidate.

A homogenous system can be described employing the gradient energy Eq. (5) and one of the multi-well potentials Eq. (11) or Eq. (12) which leads to three model parameters κ, Ω and χ defining interfacial energy γ and width l_{int}. κ denotes the gradient energy coefficient, Ω scales the multi-well barrier height and χ is a weighting factor as discussed in Sec. 2.2. Note that the order-parameter profiles at the interface are symmetrical in the homogenous case (i.e. $\eta_\beta = 1 - \eta_\alpha$ and thus intersect at $\eta_\alpha = \eta_\beta = 0.5$) only if $\chi^{\mathrm{M}} = 1.5$. Similarly, $\chi^{\mathrm{T}} = 0.5$ is necessary for the potential formulation $f_{\mathrm{well}}^{\mathrm{Toth}}$. For convenience of parameter fitting,

we restrict our investigations to cases where $\chi^{\mathrm{M}} = 1.5$ and $\chi^{\mathrm{T}} = 0.5$ in every two-phase interface which yields the two potential functions

$$f_{\mathrm{well}}^{\mathrm{Moelans}} = \frac{\tilde{\Omega}}{2}\left(\frac{3}{2}\sum_{\alpha}\sum_{\beta>\alpha}\eta_\alpha^2\eta_\beta^2 + \frac{1}{4} + \sum_{\alpha}\left(\frac{\eta_\alpha^4}{4} - \frac{\eta_\alpha^2}{2}\right)\right) \tag{15}$$

$$f_{\mathrm{well}}^{\mathrm{Toth}} = \tilde{\Omega}\left(\frac{1}{2}\sum_{\alpha}\sum_{\beta>\alpha}\eta_\alpha^2\eta_\beta^2 + \frac{1}{12} + \sum_{\alpha}\left(\frac{\eta_\alpha^4}{4} - \frac{\eta_\alpha^3}{3}\right)\right). \tag{16}$$

Both will be investigated in combination with the gradient energy Eq. (5). In non-homogenous systems, the interfacial energies can be pair-wise different which can be incorporated into MOP models with various assignment strategies. The homogenous parameters $\tilde{\kappa}$ and $\tilde{\Omega}$ can be replaced by interpolation of pairwise parameters, e.g. $\tilde{\kappa} = (\sum\kappa_{\alpha\beta}\eta_\alpha^2\eta_\beta^2)/(\sum\eta_\alpha^2\eta_\beta^2)$ [17]. This interpolation has also been used in other works [18, 33]. Other interpolation functions are not subject of this work. To correctly reproduce the interfacial energy $\gamma_{\alpha\beta}$ in any two-phase interface, it is theoretically sufficient to interpolate only one of the above parameters as $\gamma_{\alpha\beta} = \frac{1}{3}\sqrt{\kappa_{\alpha\beta}\Omega_{\alpha\beta}}$ holds. If the additional constraint of equal interfacial width for all interfaces should be fulfilled, both the gradient energy coefficient $\tilde{\kappa}$ and $\tilde{\Omega}$ need to vary spatially depending on $\boldsymbol{\eta}$. In this work, we compare three assignment strategies for parameter fitting which are summarized in Table 1 and based on the properties of a two-phase interface in Appendix A.2. The parameter ε scales the interfacial width

Table 1: Overview of assigment strategies to reproduce heterogeneous interfacial energies $\gamma_{\alpha\beta}$ between phase pairs α and β.

Strategy	gradient coeff.	barrier height	interfacial width	kinetic coeff.
κ-constant	$\tilde{\kappa} = \varepsilon\gamma_0 = \mathrm{const.}$	$\Omega_{\alpha\beta} = \frac{9\gamma_{\alpha\beta}^2}{\varepsilon\gamma_0}$	$l_{\mathrm{int}}^{\alpha\beta} = \frac{4}{3}\varepsilon\frac{\gamma_0}{\gamma_{\alpha\beta}}$	$L_{\alpha\beta} = \frac{M_{\alpha\beta}\gamma_{\alpha\beta}}{\varepsilon\gamma_0}$
l-constant	$\kappa_{\alpha\beta} = \varepsilon\gamma_{\alpha\beta}$	$\Omega_{\alpha\beta} = \frac{9\gamma_{\alpha\beta}}{\varepsilon}$	$l_{\mathrm{int}} = \frac{4}{3}\varepsilon = \mathrm{const.}$	$L_{\alpha\beta} = \frac{M_{\alpha\beta}}{\varepsilon}$
Ω-constant	$\kappa_{\alpha\beta} = \varepsilon\frac{\gamma_{\alpha\beta}^2}{\gamma_0}$	$\tilde{\Omega} = \frac{9\gamma_0}{\varepsilon} = \mathrm{const.}$	$l_{\mathrm{int}}^{\alpha\beta} = \frac{4}{3}\varepsilon\frac{\gamma_{\alpha\beta}}{\gamma_0}$	$L_{\alpha\beta} = \frac{M_{\alpha\beta}\gamma_0}{\varepsilon\gamma_{\alpha\beta}}$

and γ_0 is the reference interfacial energy. The kinetic coefficient L can be pair-wise different either due to varying phase boundary mobilities $M_{\alpha\beta}$ or due to varying interfacial width (it then becomes a function of the $\gamma_{\alpha\beta}/\gamma_0$-ratio, see Table 1). Thus, it can be re-defined in the spirit of the previous interpolation as $\tilde{L} = (\sum L_{\alpha\beta}\eta_\alpha^2\eta_\beta^2)/(\sum\eta_\alpha^2\eta_\beta^2)$. If the resulting numerical interfacial width cannot be derived analytically (i.e. $\chi^{\mathrm{M}} \neq 1.5$ or $\chi^{\mathrm{T}} \neq 0.5$), the correct fitting of $L_{\alpha\beta}$ according to physical values $M_{\alpha\beta}$ becomes a non-trivial task. In a fully variational framework, the interpolation of model parameters leads to additional terms in the evolution equation, e.g.

$$\frac{\delta f_{\mathrm{grad}}^{\mathrm{interpolated}}}{\delta\eta_\alpha} = \frac{1}{2}\frac{\partial\tilde{\kappa}}{\partial\phi_\alpha}\sum_{\alpha}|\boldsymbol{\nabla}\phi_\alpha|^2 - \boldsymbol{\nabla}\cdot(\tilde{\kappa}\boldsymbol{\nabla}\phi_\alpha) \tag{17}$$

but they are often neglected [17]. See Appendix B for an overview of variational derivatives.

2.4. Multiphase-field evolution equations

The first obvious difference between the multi-order parameter and multiphase-field approaches is the notion of ϕ_α representing the volume fraction of phase α which makes it necessary to fulfill the Gibbs simplex constraint

$$\boldsymbol{\phi} \in \mathbb{R}^N : \sum_{\alpha=1}^{N}\phi_\alpha = 1, \quad 0 \leq \phi_\alpha \quad \forall\alpha. \tag{18}$$

If the sum constraint is fulfilled and all phase fractions are larger than zero, we implicitly ensure $\phi_\alpha \in [0,1]$ $\forall\alpha = 1,\ldots,N$. Given that the initial conditions comply with Eq. (18), two conditions need to be fulfilled

during the evolution of phase-field variables, namely $\sum_{\alpha=1}^{N} \partial \phi_\alpha / \partial t = 0$ and $0 \leq \phi_\alpha$. The first condition is ensured by correctly formulating the evolution equations, either by introducing a Langrange multiplier [6]

$$\frac{\partial \phi_\alpha}{\partial t} = -L \frac{\delta f}{\delta \phi_\alpha} - \lambda \tag{19}$$

or by suitable choice of the mobility matrix which results in the sum over binary interactions as introduced by Steinbach and Pezolla [16]

$$\frac{\partial \phi_\alpha}{\partial t} = -\frac{1}{\tilde{N}\varepsilon} \sum_{\beta \neq \alpha}^{\tilde{N}} M_{\alpha\beta} \left(\frac{\delta f}{\delta \phi_\alpha} - \frac{\delta f}{\delta \phi_\beta} \right) \tag{20}$$

where $\tilde{N}$ denotes the amount of locally present phases and ε scales the interfacial width as will be shown in the following paragraph. The mobility matrix $M_{\alpha\beta}$ needs to be symmetric and all rows and columns should sum up to zero [18]. This is ensured if all entries $M_{\alpha\beta}$, $\alpha \neq \beta$ are chosen such that they match the experimental interfacial velocity of the $\alpha\beta$-phase pair, $M_{\alpha\beta} = M_{\beta\alpha}$, and the entries of the main diagonal are defined as $M_{\alpha\alpha} = -\sum_\alpha M_{\alpha\beta}$. The second criterion, $0 \leq \phi_\alpha$, is either fulfilled by construction of the energetic landscape [25] as discussed in Fig. 2 or needs to be enforced explicitly via algebraic constraints or projection schemes as discussed in Appendix D. Note that the kinetic coefficient L in Eq. (19) needs to be interpolated from pair-wise mobilities while Eq. (20) directly incorporates the physical parameters $M_{\alpha\beta}$.

Another subtle difference is that the interfacial energy terms in MPF formulations are typically formulated as the summation of binary terms which, in combination with the two-phase interface solutions from Appendix A.2, allows for re-formulation of simulation parameters. The replacement of $\kappa_{\alpha\beta} = \varepsilon \gamma_{\alpha\beta}$ and $\Omega_{\alpha\beta} = K \gamma_{\alpha\beta} / \varepsilon$ leads to an effective decoupling of interfacial energy and width which allows to keep the width of the diffuse interface constant throughout all phase pairs [6]. In this work we employ and compare the formulations

$$f_{\text{well}}^{\text{Moelans}} = \frac{9}{\varepsilon} \sum_\alpha \sum_{\beta>\alpha} \frac{3\gamma_{\alpha\beta}}{4} \phi_\alpha^2 \phi_\beta^2 + \frac{9}{2\varepsilon} \frac{\sum \gamma_{\alpha\beta} \phi_\alpha^2 \phi_\beta^2}{\sum \phi_\alpha^2 \phi_\beta^2} \left(\frac{1}{4} + \sum_\alpha \left(\frac{\phi_\alpha^4}{4} - \frac{\phi_\alpha^2}{2} \right) \right) \tag{21}$$

$$f_{\text{well}}^{\text{Toth}} = \frac{9}{\varepsilon} \sum_\alpha \sum_{\beta>\alpha} \frac{\gamma_{\alpha\beta}}{2} \phi_\alpha^2 \phi_\beta^2 + \frac{9}{\varepsilon} \frac{\sum \gamma_{\alpha\beta} \phi_\alpha^2 \phi_\beta^2}{\sum \phi_\alpha^2 \phi_\beta^2} \left(\frac{1}{12} + \sum_\alpha \left(\frac{\phi_\alpha^4}{4} - \frac{\phi_\alpha^3}{3} \right) \right) \tag{22}$$

$$f_{\text{well}}^{\text{Garcke}} = \frac{9}{\varepsilon} \sum_\alpha \sum_{\beta>\alpha} \gamma_{\alpha\beta} \phi_\alpha^2 \phi_\beta^2 + \frac{9}{\varepsilon} \sum_\alpha \sum_{\beta>\alpha} \sum_{\gamma>\beta} \gamma_{\alpha\beta\gamma} \phi_\alpha^2 \phi_\beta^2 \phi_\gamma^2 \tag{23}$$

$$f_{\text{ob}} = \frac{16}{\varepsilon \pi^2} \sum_\alpha \sum_{\beta>\alpha} \gamma_{\alpha\beta} \phi_\alpha \phi_\beta \tag{24}$$

where the prefactors $K = 9$ for the multi-well and $K = 16/\pi^2$ for the multi-obstacle formulation ensure that the parameter $\gamma_{\alpha\beta}$ corresponds to the physical interfacial energy of the α-β phase pair. Eq. (21)-(24) will be studied in combination with the two gradient formulations Eq. (6) and (7). The factors in Eqs. (21) and (22) are chosen such that in every two-phase interface $\chi^{\text{M}} = 1.5$ and $\chi^{\text{T}} = 0.5$ are fulfilled.

3. Analytics of triple junctions for our validation cases

3.1. Grain-boundary geometry in static equilibrium

At triple lines, each pair-wise isotropic interfacial energy leads to a force (per unit length) that acts tangentially on the surface and hence normal to the direction of the triple-line element (see Fig. 3a). The force magnitude scales with the respective interfacial energy. Neglecting the line tension of the triple line and non-equilibrium contributions such as by a finite triple-junction mobility, the balance of forces results in an equilibrium condition at the triple junction which can be expressed as [15, p. 379]

$$\sum_{\alpha,\beta \in \mathcal{T}, \alpha<\beta} \gamma_{\alpha\beta} \boldsymbol{t}_{\alpha\beta} = \boldsymbol{0}. \tag{25}$$

10

Here, $\mathcal{T} = \{1, 2, 3\}$ is the set of occurring phases, $\boldsymbol{t}_{\alpha\beta}$ is the unit vector tangential to the $\alpha\beta$ interface and pointing away from the triple line, normal to the unit vector pointing along the triple line $\boldsymbol{t}_{\text{TL}}$, i.e. $\boldsymbol{t}_{\alpha\beta} \cdot \boldsymbol{t}_{\text{TL}} = 0$. Analogously, we can re-write the force balance in terms of unit normal vectors $\boldsymbol{n}_{\alpha\beta} = \boldsymbol{t}_{\alpha\beta} \times \boldsymbol{t}_{\text{TL}}$ which yields $\sum \gamma_{\alpha\beta} \boldsymbol{n}_{\alpha\beta} = \boldsymbol{0}$. Applying a dot product with $\boldsymbol{n}_{12}$ to Eq. (25), one can eliminate $\gamma_{12} \boldsymbol{t}_{12}$ and obtain a scalar equation that reads

$$\gamma_{13} \cos\left(\boldsymbol{n}_{12} \angle \boldsymbol{t}_{13}\right) + \gamma_{23} \cos\left(\boldsymbol{n}_{12} \angle \boldsymbol{t}_{23}\right) = 0 \,. \tag{26}$$

With the angles defined in Fig. 3a, i.e. $\boldsymbol{n}_{12} \angle \boldsymbol{t}_{13} = \theta_{23} + \pi/2$ and $\boldsymbol{n}_{12} \angle \boldsymbol{t}_{23} = \theta_{13} - \pi/2$, one finds

$$\frac{\gamma_{23}}{\sin\left(\theta_{23}\right)} = \frac{\gamma_{13}}{\sin\left(\theta_{13}\right)} \,, \tag{27}$$

where $\theta_{\alpha\beta}$ denotes the dihedral angle opposite to the $\alpha\beta$ interface (measured in the plane normal to $\boldsymbol{t}_{\text{TL}}$). Repeating this procedure with one of the other two normal vectors finally yields the set of equations

$$\frac{\gamma_{12}}{\sin\left(\theta_{12}\right)} = \frac{\gamma_{13}}{\sin\left(\theta_{13}\right)} = \frac{\gamma_{23}}{\sin\left(\theta_{23}\right)} \tag{28}$$

which is well-known as Young's law.

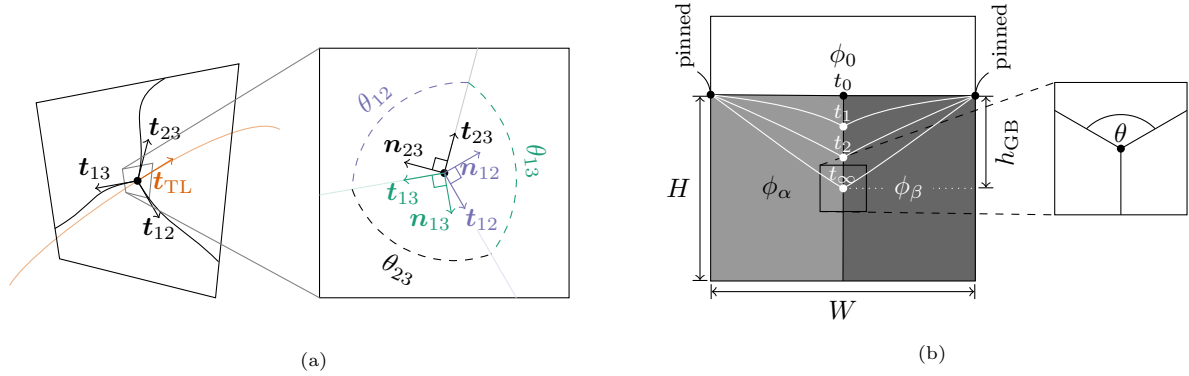(a)   (b)

Figure 3: General case of the interfacial-energy force balance at a triple line including tangential and normal vectors as well as dihedral angles shown in a). Subfigure b) illustrates the initial simulation setup where white lines exemplarily show the evolution towards static equilibrium for the first benchmark.

For our validation, we employ the two-dimensional setup shown in Fig. 3b. We assume two of the three interfacial energies to be equal, i.e. $\gamma_{\alpha 0} = \gamma_{\beta 0} = \gamma_0$ and the third $\gamma_{\alpha\beta}$ will be varied. This problem is thus well described by one angle

$$\theta = \theta_{\alpha\beta} = 2\arccos\left(\frac{\gamma_{\alpha\beta}}{2\gamma_0}\right). \tag{29}$$

In equilibrium, surfaces form straight lines due to energy minimization and, thus, the dihedral angle can be expressed in terms of the triple point position h_{GB}

$$\theta = 2\arctan\left(\frac{W}{2h_{\text{GB}}}\right) \tag{30}$$

and hence

$$h_{\text{GB}} = W \frac{\gamma_{\alpha\beta}}{2\sqrt{4\gamma_0^2 - \gamma_{\alpha\beta}^2}} \,. \tag{31}$$

11

As we are interested in the total interfacial energy of the system, the length of each interface is multiplied with the corresponding energy. The length of the vertical GB equals

$$l_{\alpha\beta} = H - h_{\mathrm{GB}} = W \left(\frac{H}{W} - \frac{\gamma_{\alpha\beta}}{2\sqrt{4\gamma_0^2 - \gamma_{\alpha\beta}^2}} \right) \tag{32}$$

and the diagonal grain boundaries have lengths

$$l_0 = l_{\alpha 0} = l_{\beta 0} = \sqrt{\frac{W^2}{4} + h_{\mathrm{GB}}^2} = W \frac{\gamma_0}{\sqrt{4\gamma_0^2 - \gamma_{\alpha\beta}^2}} \tag{33}$$

which follows from Eq. (31). The total interfacial energy of the system is given by

$$E_{\mathrm{total}} = l_{\alpha\beta}\gamma_{\alpha\beta} + 2l_0\gamma_0 = W \left(\frac{H}{W}\gamma_{\alpha\beta} + \sqrt{\gamma_0^2 - \frac{\gamma_{\alpha\beta}^2}{4}} \right) . \tag{34}$$

3.2. Grain-boundary geometry in steady state motion

For the second validation case, we are interested in the steady-state motion of a curved grain boundary (GB), symmetrically centered between two vertical grain boundaries as shown in Fig. 4, moving with a constant vertical velocity V. The value of V is initially unknown and will be part of the derivation. The derivation closely resembles the one shown in Gottstein and Shvindlerman [15, p. 384], although the authors discuss the result in a different context and formulate the solution inversely (solve for $x(y)$ instead of $y(x)$). An almost identical derivation to the one shown is given in an early work of Mullins [28]. Nevertheless, we highlight the necessary steps to keep the document self-contained. If we assume the GB to have an isotropic grain-boundary energy γ_0 (in $\mathrm{J\,m^{-2}}$) and isotropic mobility M_0 (in $\mathrm{m^4/J/s}$), the normal velocity v_n is proportional to its curvature κ, i.e. obeys the governing equation

$$v_n = M_0\gamma_0\kappa \tag{35}$$

in the absence of bulk driving forces. Note that the signs of v_n and κ are defined such that the movement is towards the center of curvature. If the geometry of the grain boundary is given by function $y(x)$, where
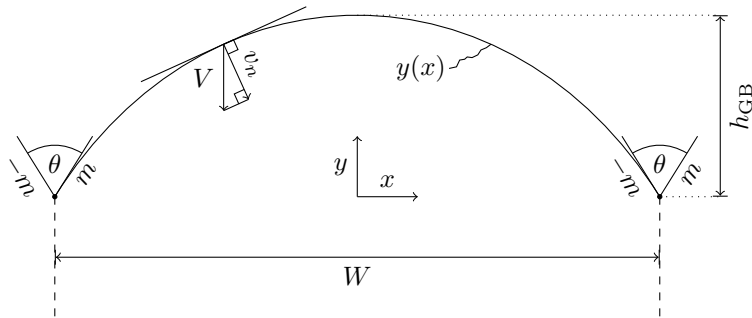

Figure 4: Schematic of the considered grain-boundary geometry. Relevant quantities occuring in the following derivations are labeled in the sketch.

x is the horizontal and y the vertical coordinate, the curvature can be expressed by its first two derivatives

$$\kappa = -\frac{y''(x)}{\left(1 + (y'(x))^2\right)^{3/2}}. \tag{36}$$

12

To fix the grain boundary in the moving frame of reference, we set the position of the triple junctions at $x = \pm W/2$ to zero such that $y(\pm W/2) = 0$. The slope of the grain boundary at these points is constant $m = \cot(\theta/2)$ according to Young's law and given in terms of the dihedral angle θ which yields $y'(-W/2) = m$ and $y'(W/2) = -m$. Note that v_n is only equal to V for $\theta = 180°$ or at $x = 0$, but is more generally described by the Pythagorean theorem as

$$V = v_n \sqrt{1 + (y'(x))^2}. \tag{37}$$

Combining Eqs. (35) - (37), the general problem can be expressed as an ordinary differential equation

$$y''(x) = -\frac{V}{M_0\gamma_0}\left(1 + (y'(x))^2\right). \tag{38}$$

Details for solving this equation are given in Appendix E.1. The steady-state velocity is then obtained as

$$V = \frac{2M_0\gamma_0}{W}\arctan(m). \tag{39}$$

For $m \ll 1$ (and thus $\arctan(m) \approx m$), Eq. (39) reduces to the small-slope approximation $V/m \approx 2M_0\gamma_0/W$. Additionally, one may express the velocity in terms of θ by $\arctan(m) = \pi/2 - \theta/2$, which results in the remarkably simple form

$$V = \frac{M_0\gamma_0}{W}(\pi - \theta). \tag{40}$$

A comparison of the interface velocities from the small-slope approximation and the general formula is shown in Fig. 5a. The solution of Eq. (38) subject to the mentioned boundary conditions can be written as

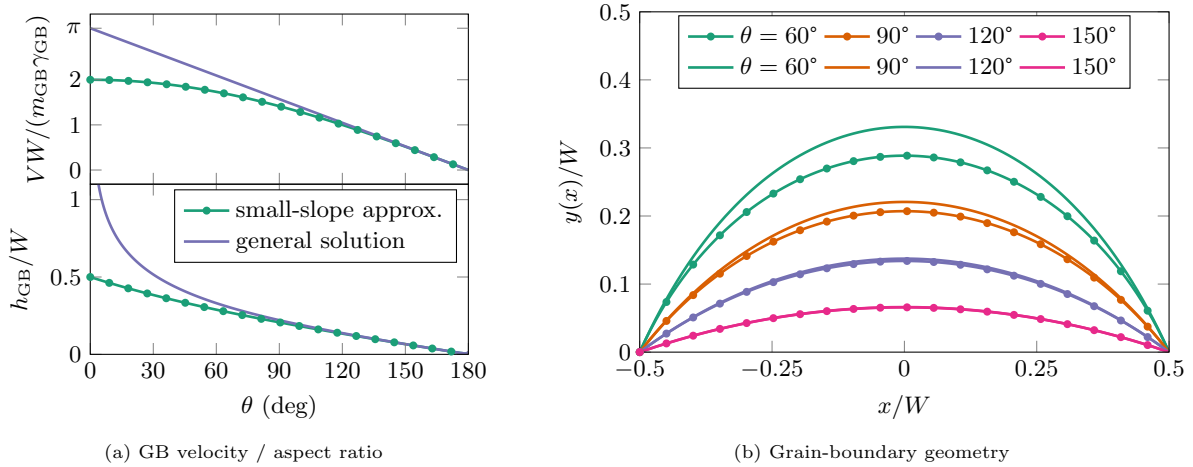(a) GB velocity / aspect ratio

(b) Grain-boundary geometry

Figure 5: Comparison of the small-slope approximation (dotted lines) and the exact analytical solution (solid lines) of the grain-boundary a) velocity (exact Eq. (40) and small-slope Eq. (E.13)) and b) resulting geometries for varying triple-junction angles θ.

$$y(x) = \frac{W}{\pi - \theta}\ln\left(\frac{\cos\left(\frac{\pi-\theta}{W}x\right)}{\sin\left(\frac{\theta}{2}\right)}\right). \tag{41}$$

The resulting geometries are shown in Fig. 5b in comparison with the results obtained from the small-slope approximation. An interesting result is that the aspect ratio of the GB $h_{\mathrm{GB}}/W = y(0)/W$ is related to the dihedral angle as follows

$$\frac{h_{\mathrm{GB}}}{W} = \frac{\ln\left(\sin\left(\theta/2\right)\right)}{\theta - \pi}. \tag{42}$$

We use this expression to determine the resulting dihedral angle from simulations.

13

4. Simulation studies

4.1. Simulation setup

For our benchmark problem, we start with physical values in the order of typical microstructure simulations listed in Table 2 and make them non-dimensional, as would be common practice for any application to a specific material system. Three reference quantities are applied to de-dimensionalize the problem, namely the reference time $t_{\mathrm{ref}} = 100\,\mathrm{s}$, length $x_{\mathrm{ref}} = 1\,\mu\mathrm{m} = 10^{-6}\,\mathrm{m}$ and energy $\Omega_{\mathrm{ref}} = 10^6\,\mathrm{J/m^3}$, which yields

$$\tilde{W} = \frac{W}{x_{\mathrm{ref}}}, \quad \tilde{\gamma}_{\alpha\beta} = \frac{\gamma_{\alpha\beta}}{\Omega_{\mathrm{ref}}x_{\mathrm{ref}}} \quad \text{and} \quad \tilde{M} = M\frac{\Omega_{\mathrm{ref}}t_{\mathrm{ref}}}{x_{\mathrm{ref}}}. \tag{43}$$

Note that the choice of parameters is somewhat arbitrary and the simulation results could be re-scaled differently by changing the reference values.

The initial conditions of the problem are identical for the two following sub-problems. They are sketched in Fig. 3b and can be summarized as follows: We start with initially sharp interfaces and fill $0 \leq x \leq W$ and $80 < y \leq 100$ with $\phi_0 = 1$ and, furthermore, $0 \leq x \leq W/2$ and $0 \leq y \leq 80$ with $\phi_\alpha = 1$ and the other half $W/2 < x \leq W, 0 \leq y \leq 80$ with $\phi_\beta = 1$. The respective other phases are equal to zero. A similar validation example has been used in [42]. For all cases, we employ Neumann boundary conditions (BCs) $\boldsymbol{\nabla}\phi_\alpha \cdot \vec{n} = 0$, $\forall\alpha$ at the top and bottom of the domain. At the left and right domain boundary

- Dirichlet BCs are used for sub-problem (1) according to the initial setup, i.e. phase boundaries are pinned at $[0, 80]$ and $[W, 80]$;

- Neumann BCs with $\boldsymbol{\nabla}\phi_\alpha \cdot \vec{n} = 0$, $\forall\alpha$ are used for subproblem (2) which in this case reflects mirror symmetry. Alternatively, the domain length can be doubled to $2W$ in combination with periodic BCs.

Table 2: Set of simulation parameters

Parameter	Symbol	Physical value	Simulation value
Width of domain	W	$100\,\mu\mathrm{m}$	100
Height of domain	H	$[100,\dots,400]\,\mu\mathrm{m}$	$[100,\dots,400]$
Spatial resolution	Δx	W/cells	1
Interfacial energy	$\gamma_{\alpha0} = \gamma_{\beta0} = \gamma_0$	$1.0\,\mathrm{J/m^2}$	1.0
	$\gamma_{\alpha\beta}$	$[0.1,\dots,2.0]\gamma_{\alpha0}\,\mathrm{J/m^2}$	$[0.01,2.0]$
Mobility	$M_{\alpha0} = M_{\beta0} = M_0$	$10^{-14}\,\mathrm{m^4/(Js)}$	1
	$M_{\alpha\beta}$	$10^{-14}\,\mathrm{m^4/(Js)}$	1

All simulations are conducted using codes based on finite difference stencils and an explicit Euler time-stepping. MPF simulations were performed using PACE3D [36, 43] which is an in-house code. Furthermore, all the models (MOP as well as MPF) were implemented for the specific case of three phases in MATLAB together with the necessary post-processing tools to acquire the metrics presented in the following sections. The MATLAB code has been made publicly available [44].

4.2. Static triple junction

The first benchmark case employed in this work is a triple junction that reaches a static equilibrium as sketched in Fig. 3b and 6. Below, the metrics for quantitative comparison of the various model formulations with the analytical considerations in Sec. 3.1 are defined:

14

- The **total interfacial energy** is computed as the energy density integral over the simulation domain, and its total value is compared to the sharp interface solution from Eq. (34). Convergence to equilibrium state is quantified by the relative energy change over time $\epsilon = |\mathcal{F}^n - \mathcal{F}^{n-1}|/\mathcal{F}^n$ and all the simulations presented are below a threshold of $\epsilon = 10^{-5}$;

- The **dihedral angle** θ of the triple junction is computed from the position of the triple point (Eq. (30)) and compared with the analytical solution from Young's law in Eq. (29). The numerical triple point is defined as the intersection of isolines $\phi_0 = \phi_\alpha$ and $\phi_0 = \phi_\beta$;

- Spurious occurance of ϕ_α, ϕ_β and ϕ_0 in the respective other two-phase interface is quantified as the **maximum value of the phase** as shown in Fig. 6.

As the domain height H limits the range of observable triple junction angles, we conduct simulation studies with $H = 100$ and $H = 200$. The results are equal within the applicable range of $\gamma_{\alpha\beta}$ values. The temporal evolution towards equilibrium is shown exemplarily in Fig. 6.
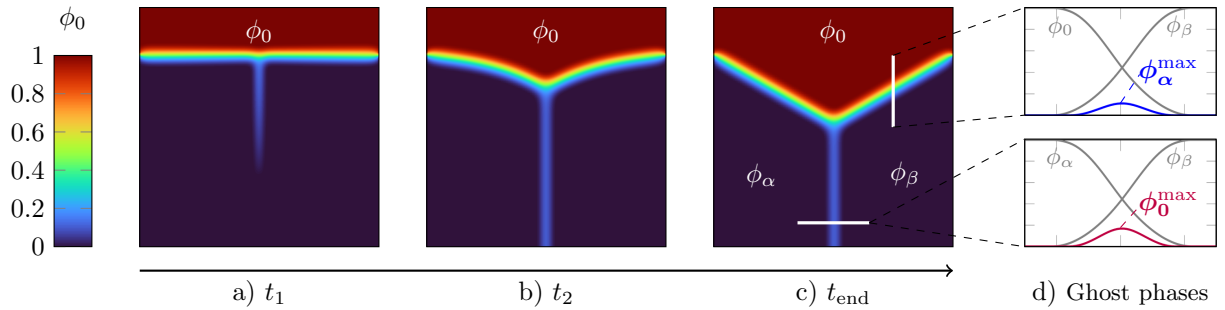

Figure 6: Evolution of phase ϕ_0 towards static equilibrium shown exemplarily for $\gamma_{\alpha\beta} = \gamma_0$ and domain size 100×100. Subfigures show a) state close to the initial conditions, b) an in-between state and c) the final state in equilibrium. Spurious phases are quantified by occurance in the respective other two-phase interface as sketched by linescans in c) and the detailed plots in d).

We start with a comparison of MOP models. As the evolution of order parameters is not directly coupled, the potential function needs to provide stable equilibria for $\eta = 0$ and $\eta = 1$ which excludes the obstacle potential. Furthermore, simulations based on formulation $f_{\mathrm{well}}^{\mathrm{Garcke}}$ (Eq. (10)) exhibit large areas where all three order parameters are equal zero $\eta_\alpha = \eta_\beta = \eta_\gamma = 0$ which cannot be interpreted in a physically meaningful manner. Therefore, it is not applicable to the framework of MOP models. It seems that the single phase monomials in $f_{\mathrm{well}}^{\mathrm{Moelans}}$ and $f_{\mathrm{well}}^{\mathrm{Toth}}$ are a necessary prerequisite for MOP models. Similarly, the two gradient formulations based on binary contributions (Eqs. (6) and (7)) fail at producing reasonable results which reduces the possible model choices to gradient term Eq. (5) in combination with the potential functions $f_{\mathrm{well}}^{\mathrm{Moelans}}$ ((15)) and $f_{\mathrm{well}}^{\mathrm{Toth}}$ ((16)). An overview of all model combinations employed in this work with references to the original works is given in Table 3.

Table 3: Overview of model combinations employed in this work with references to original works. All new combinations are marked as such.

		$f_{\mathrm{well}}^{\mathrm{Moelans}}$	$f_{\mathrm{well}}^{\mathrm{Toth}}$ 1	$f_{\mathrm{well}}^{\mathrm{Garcke}}$	f_{obstacle}
MOP	$f_{\mathrm{grad}}^{\mathrm{interpolate}}$ Eq. (5)	[3, 17]	new	X	X
MPF	$f_{\mathrm{grad}}^{\mathrm{dot}}$ Eq. (6)	new	new	new	[16, 21]
	$f_{\mathrm{grad}}^{\mathrm{weighted}}$ Eq. (7)	new	new	[6, 24]	[6, 24]

15

The mutual comparison of two well formulations together with the three assignment strategies (see Table 1) yields six combinations. We use γ_0 from Table 2 as the reference value and $\varepsilon = 5\Delta x$ for the parameter fitting outlined in Table 1. This results in a constant interfacial width of 6.67 in the $\alpha 0$- and $\beta 0$-interfaces while the $\alpha\beta$-interface scales with the $\gamma_{\alpha\beta}/\gamma_0$-ratio for all cases where κ or Ω are constant. The results in Fig. 7 show that all six model variants reproduce the analytic solutions with little error in the range of $\gamma_{\alpha\beta}/\gamma = [0.75, 1.25]$ which can be attributed to the absence of spurious phases. For the ratios of 0.5 and 1.5, only a small fraction of spurious phases occurs and the results match reasonably well with analytics. For $\gamma_{\alpha\beta}/\gamma_0 = 0.1$ and $= 0.25$ the simulations with parameter fitting based on Ω-constant are
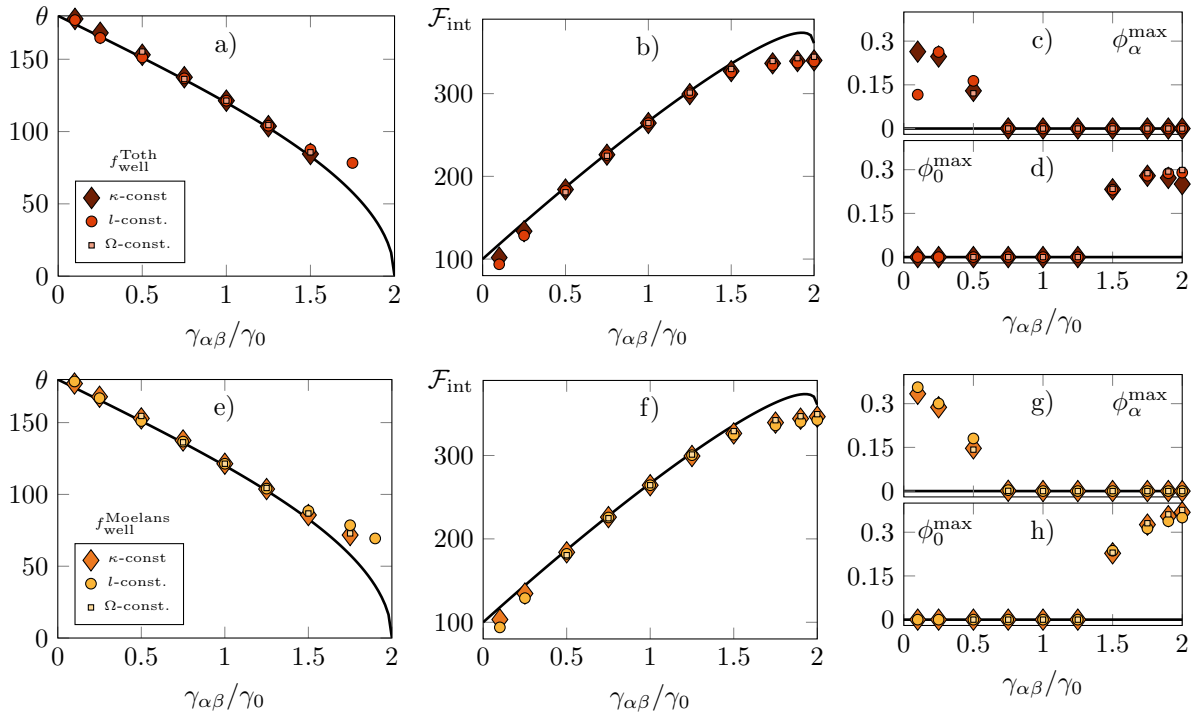

Figure 7: MOP comparison of metrics for the static triple junction with 100×200 domain size. The studies encompass gradient formulation Eq. (5) in combination with two well potentials. Simulations in subfigures a)-d) were performed with $f_{\text{well}}^{\text{Toth}}$ (red markers) while $f_{\text{well}}^{\text{Moelans}}$ has been used in subfigure e)-h) (orange markers). The three assignment strategies from Tab. 1 are marked as indicated by the legend in a) and e). These legends apply to all plots in the respective row. Analytical solutions are shown as black lines.

numerically instable in our case as the interfacial width is reduced to $\approx \Delta x$. This issue can be addressed by global mesh refinement, discretization schemes that allow for local mesh refinement or adjusting the parameter assignment. In any case, the resolution of interfacial widths that vary by an order of magnitude comes with additional computational cost which is the biggest drawback of assignment strategies that do not keep l_{int} constant. Furthermore, the diffuse interface needs to be resolved with enough grid points to reduce the discretization error as has been nicely illustrated by Eiken [29]. For high $\gamma_{\alpha\beta}/\gamma$-ratios, the large fraction of ϕ_0 in the $\alpha\beta$-interface leads to a deviation of the overall system free energy and, furthermore, hinders the motion of the triple junction. Above a certain $\gamma_{\alpha\beta}/\gamma$-ratio, the observed angle is larger than the analytically expected one, however, it cannot be evaluated with the metrics defined above. Due to the large fraction of ghost phases, the isolines $\phi_0 = \phi_\alpha$ and $\phi_0 = \phi_\beta$ do not intersect anymore such that the actual position of the triple junction becomes numerically ill-defined. Consequently, the data points are missing

---

[1]In the original work [18], this potential term has been combined with the gradient term $f_{\text{grad}}^{\text{interpolate}}$ within the MPF framework. This combination is not covered within this paper.

in the left column plots of Fig. 7. Overall, the difference between the well formulations and the various assignment strategies is surprisingly small. Spurious phases can be generated by both the gradient term $f_{\text{grad}}^{\text{interpolate}}$ and the potential as all three assignment strategies result in a similar amount of spurious phases. None of the model combinations captures de-wetting at $\gamma_{\alpha\beta}/\gamma_0 = 2$.

For the multiphase-field method, we compare the eight possible combinations of the gradient formulations Eq. (6) and (7) and the potentials Eq. (21)-(24). The numerical parameter ε scales the width of the diffuse interface and is set to 5, which corresponds to $10 - 12$ grid points within the diffuse interface region. To check the influence of ε with regard to the overall domain width W, a comparative study has been carried out with a grid resolution of 0.5 which corresponds to a 200×400 grid and $\varepsilon = 2.5$. The differences in total energy and dihedral angle were found to be below 1%. The results in Fig. 8 clearly show that the deviations of the dihedral angle and total free energy from the analytic solutions are directly linked to the occurrence of spurious phases. Generally, all combinations including the gradient term $f_{\text{grad}}^{\text{weighted}}$ (denoted by circular markers) show larger deviation from the analytical solutions and higher fractions of ghost phases. We conclude that the driving force resulting from the functional derivative of Eq. (7) is one possible source of spurious phase generation. Furthermore, it should be noted that the implementation of the functional derivative of $f_{\text{grad}}^{\text{weighted}}$ contains about 20 times more arithmetic operations, thus resulting in simulation times that are significantly longer than the equivalent potential term combined with the gradient formulation $f_{\text{grad}}^{\text{dot}}$.
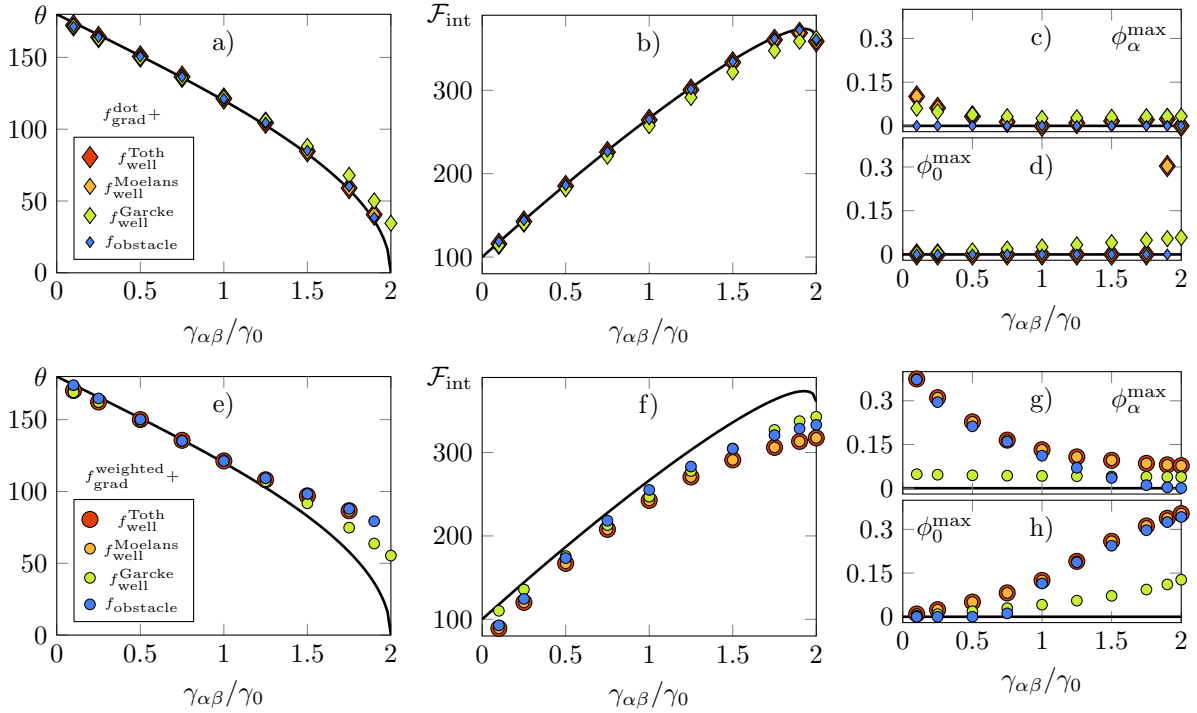

Figure 8: MPF comparison of metrics for the static triple junction with 100×200 domain size. Combinations including $f_{\text{grad}}^{\text{dot}}$ are marked by diamonds and shown in a)-d) while $f_{\text{grad}}^{\text{weighted}}$ is denoted by circles in subfigures e)-h). The potential terms are color coded as indicated by the legend ($f_{\text{well}}^{\text{Toth}}$=red,$f_{\text{well}}^{\text{Moelans}}$=orange,$f_{\text{well}}^{\text{Garcke}}$=green,$f_{\text{obstacle}}$=blue). Analytical solutions are shown as black lines.

As discussed in Sec. 2.2, the potential formulation $f_{\text{well}}^{\text{Garcke}}$ tends to energetically favor triple phase regions over two-phase interphases which results in spurious phases and a deviation from the analytical solutions. The fraction of ghost phases can be reduced by increasing the numerical parameter $\Omega_{\alpha\beta\gamma}$ which scales the triplet energy contribution. The parameter study in Fig. 9 shows that for small values of $\Omega_{\alpha\beta\gamma}$, a high fraction of spurious phases distorts the equilibrium solutions. Very high values of $\Omega_{\alpha\beta\gamma}$ result in numerical

pinning (i.e. the triple junction does not move) such that the resulting dihedral angle is $\approx 180°$ for all $\gamma_{\alpha\beta} \in [0, 2]$. For this benchmark, we found that a value of $\Omega_{\alpha\beta\gamma} = 100\,\Omega_{\alpha\beta}$ yields the best solution (see results Fig. 9). Nevertheless, the combination of $f_{\mathrm{grad}}^{\mathrm{dot}}$ and $f_{\mathrm{well}}^{\mathrm{Garcke}}$ generally exhibits larger deviation from the analytical solution than combination with the other two potential terms. This can be traced back to the higher amount of spurious phases resulting from the potential term. Only three combinations effectively suppress spurious phases over a large range of $\gamma_{\alpha\beta}/\gamma_0$-ratios, namely the gradient term $f_{\mathrm{grad}}^{\mathrm{dot}}$ in combination with the well potentials $f_{\mathrm{well}}^{\mathrm{Toth}}$ and $f_{\mathrm{well}}^{\mathrm{Moelans}}$ or with the obstacle potential f_{obstacle}. Consequently, these are also the only three combinations which correctly capture de-wetting of the α and β phase for $\gamma_{\alpha\beta}/\gamma_0 = 2$. Results obtained from $f_{\mathrm{well}}^{\mathrm{Toth}}$ and $f_{\mathrm{well}}^{\mathrm{Moelans}}$ differ less than 1% due to the fact that for $\chi^{\mathrm{T}} = 0.5$ and $\chi^{\mathrm{M}} = 1.5$ the energetic landscapes are identical.
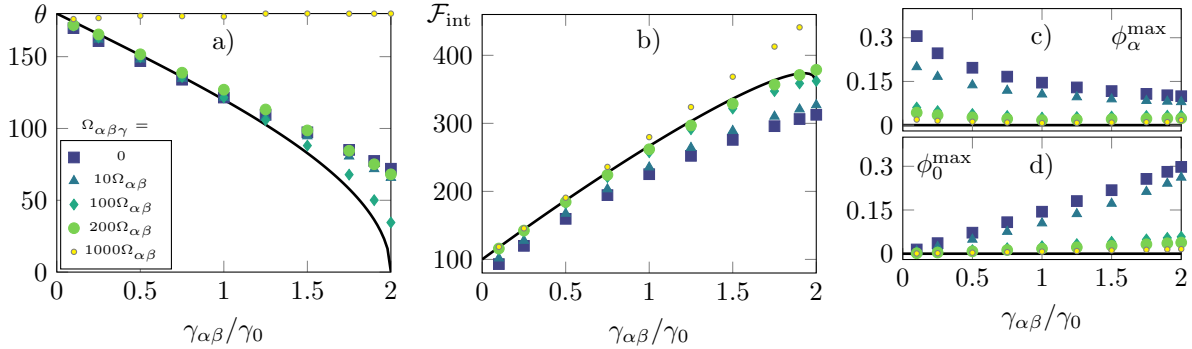

Figure 9: Influence of numerical parameter $\Omega_{\alpha\beta\gamma}$ in $f_{\mathrm{well}}^{\mathrm{Garcke}}$ (Eq. (10)) on spurious phase generation and model error. Simulations were performed employing $f_{\mathrm{grad}}^{\mathrm{dot}}$. Analytical solutions are shown as black lines.

There are many works that employ the second gradient formulation $f_{\mathrm{grad}}^{\mathrm{weighted}}$ in combination with a modified obstacle potential [6, 10, 42]. Similarly to the study in Fig. 9, a triplet term $\Omega_{\alpha\beta\gamma}\phi_\alpha\phi_\beta\phi_\gamma$ can be introduced to counteract the spurious phases generated from the functional derivative of the gradient term. The publication by Hötzer *et al.* [42] is dedicated to the calibration of the numerical parameter $\Omega_{\alpha\beta\gamma}$, in which the authors conclude that, first of all, it largely influences the equilibrium contact angles and, secondly, strongly depends on the specific pair-wise interfacial energies in every triple junction. This, together with the fact that for many phases N there could theoretically be $\propto N^3$ fitting parameters $\Omega_{\alpha\beta\gamma}$, makes this approach very complicated and numerically inefficient. Note that the initial problem is the occurance of spurious phases which can more efficiently be addressed by replacing $f_{\mathrm{grad}}^{\mathrm{weighted}}$ with $f_{\mathrm{grad}}^{\mathrm{dot}}$.

4.3. Steady-state motion of a triple junction

The second benchmark is a triple junction in steady-state motion which results from the first benchmark with modified BCs on the left and right boundary. The relevant metrics for quantitative comparison are

- The **dihedral angle** is computed from the height of the profile h_{GB} using the analytic expression (42). h_{GB} is measured as the distance between the interface position at the left boundary $y_{\phi_0 = \phi_\alpha}^{x=0}$ (or right boundary as the problem setup is symmetric) and the y-coordinate of the triple point. Convergence to steady-state is quantified by the temporal change of the profile height with respect to the domain width $\epsilon = |h_{\mathrm{GB}}^n - h_{\mathrm{GB}}^{n-1}|/W$;

- The **velocity** is measured as the temporal change of the y-coordinate of the interface at the left boundary $V = |(y_{\phi_0=\phi_\alpha}^{x=0})^n - (y_{\phi_0=\phi_\alpha}^{x=0})^{n-1}|/\Delta t$;

- The **(mis-)match of numerical results for the grain boundary geometry** with regard to the analytical solution (Eq. (41)) is quantified by a relative error measure introduced by the L^2-norm as

  $\mathrm{L2} = \|y_{\mathrm{numeric}} - y_{\mathrm{analytic}}\|_2 = \frac{1}{W}\sqrt{\frac{1}{N}\sum_{i=1}^{N}(y_i^{\mathrm{numeric}} - y_i^{\mathrm{analytic}})^2}$

where y_{numeric} and y_{analytic} are both discrete representations evaluated at the same nodes in x-direction. The reference for the y-values of the GB profile is set to zero at the left and right boundary, i.e. $y_{\phi_0 = \phi_\alpha}^{x=0} = 0$.

For MOP simulations, we employ the same model variants as in the first benchmark. The results shown in the first row of Fig. 10 are consistent with the results obtained from the static triple junction case. All model variations match the analytic reference reasonably well within the range of $\gamma_{\alpha\beta}/\gamma_0 \in [0.5, 1.5]$. For the ratio of 0.1 numerical pinning is observed which results in an angle close to $180°$ and a velocity which is lower than the analytically expected one. For high $\gamma_{\alpha\beta}/\gamma_0$-ratios, on the other hand, large deviation from the reference solution can be observed which, again, can be traced back to the occurrence of spurious phases distorting the equilibrium angles as well as the kinetics of the triple junction.
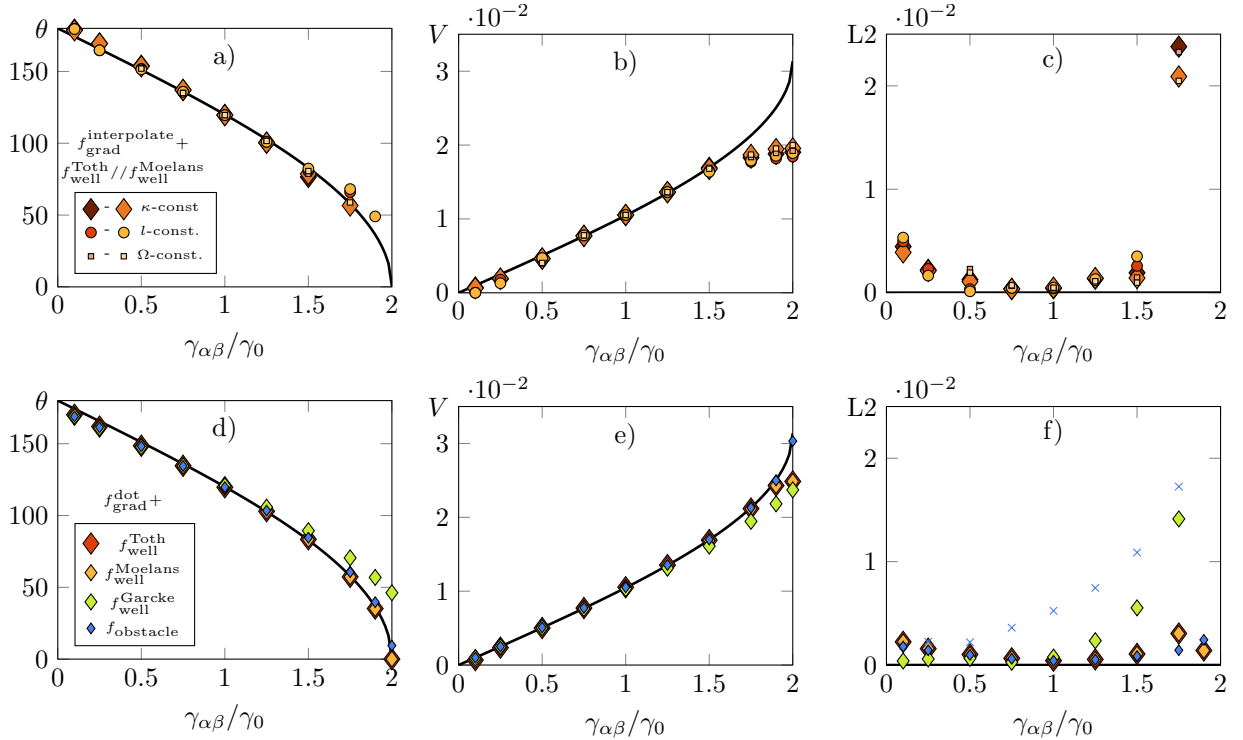

Figure 10: MOP and MPF comparison of metrics for the steady-state triple junction. The potential terms are color coded as indicated by the legend ($f_{\text{well}}^{\text{Toth}}$=red,$f_{\text{well}}^{\text{Moelans}}$=orange,$f_{\text{well}}^{\text{Garcke}}$=blue,$f_{\text{obstacle}}$=green). The top row shows MOP results obtained with gradient term $f_{\text{grad}}^{\text{interpolate}}$ and three different assignment strategies. All MPF simulations in the bottom row are done in combination with the gradient term $f_{\text{grad}}^{\text{dot}}$. Analytical solutions are shown as black lines.

On the MPF side, we compare four model variants, namely all four potential terms Eqs. (21)-(24) in combination with $f_{\text{grad}}^{\text{dot}}$. At this point we exclude the other gradient term $f_{\text{grad}}^{\text{weighted}}$ due to the previous results. Similar to the previous benchmark, the well-potential $f_{\text{well}}^{\text{Garcke}}$ shows the largest deviation from the analytical solution due to appearance of spurious phases. Furthermore, the triplet term scaled by $\Omega_{\alpha\beta\gamma}$ exhibits a drag force on the triple junction as discussed by Eiken [29]. As discussed before, large values of $\Omega_{\alpha\beta\gamma}$ (yellow dots in Fig. 9) lead to pinning of the triple junction which is the extreme case of this drag effect. The other three model combinations yield a close match with the analytical solutions. One peculiarity of the obstacle potential can be seen in the L2-norm results in Fig. 10. Due to the finite interface width, the choice of $\varepsilon = 5\Delta x$ can lead to 12 or 13 grid points within the diffuse interface where the second is slightly favorable energetically. This leads to a symmetry breaking force and the x-position of the TP tends to stabilize at 49.5 or 50.5. This numerical issue can be circumvented if ε is chosen such that the interface

19

width to Δx ratio corresponds to an integer, e.g. $\varepsilon = 4 \cdot 12\Delta x/\pi^2 \approx 4.8634\Delta x$. The results for the dihedral angle and velocity are almost identical but the L2-norm differs drastically due to the shift in GB geometry. To illustrate the effect we plot results obtained with $\varepsilon = 4.8634\Delta x$ as blue diamonds and $\varepsilon = 5\Delta x$ using blue crosses.

5. Conclusion

The triple junction has been established as a well-defined benchmark for quantitative comparison of various multiphase-field and multi-order parameter models. Thorough analytical consideration as well as problem-specific metrics lay the foundation for quantitative comparison. The systematic combination of various gradient and potential formulations yields new insights into the influence on generation of spurious phases which we identify as the main source for model error. The proposed benchmark is simple enough to be highly reproducible and yet captures most critical aspects of capillary effects in multi-phase systems.

The simulation studies show that the generation of spurious phases is directly linked to a deviation from analytic solutions. Possible sources for ghost phases can come from both the gradient and potential energy contribution and are unraveled by systematic combination of these terms. All MOP model variants yield similar results despite the differences between potential terms and parameter assignment strategies. All of them reproduce the analytic solutions with little model error for surface energy ratios around one which makes them especially attractive for the simulation of systems with small heterogeneity. However, they fail at reproducing correct triple junction angles for extreme ratios $\gamma_{\alpha\beta}/\gamma_0$. None of the model variants under investigation is able to capture de-wetting for $\gamma_{\alpha\beta}/\gamma_0 = 2$. Other parameter assignment strategies or re-formulation of the gradient term might offer a solution in these cases.

For the MPF models, the studies reveal that $f_{\text{grad}}^{\text{weighted}}$ generally performs worse than $f_{\text{grad}}^{\text{dot}}$ as it introduces an additional source of spurious phases. The two well-potentials $f_{\text{pot}}^{\text{Toth}}$ and $f_{\text{pot}}^{\text{Moelans}}$ yield almost the same results and, overall, coincide with analytical solutions. The third well-potential $f_{\text{pot}}^{\text{Garcke}}$ leads to a higher fraction of ghost phases and, thus, deviates more strongly from the reference solution. The obstacle potential results in a close match with analytical solutions and, in our case, comes with an advantage in computational efficiency. The first reason for this is the simple form of the respective variational derivative and, secondly, as the equilibrium profile is given by a sinus function, the interface has a finite width and computation of phase evolution can be reduced to cells that exhibit a spatial gradient in phase-field values. Note that this computational advantage cannot be generalized because computational efficiency results from a complex interplay of numerical implementation, time stepping and the inclusion of the Gibbs simplex constraint.

By comparing the results obtained from both model families, MPF and MOP, it becomes evident that application of the Gibbs simplex constraint allows for a wider range of potential formulations but adds more computational complexity. For MPF models it seems preferable to formulate energetic contributions in terms of pairwise interaction terms as the evolution equations reflect this dual nature as well. This allows for simulation of high $\gamma_{\alpha\beta}/\gamma_0$- as well as $M_{\alpha\beta}/M_0$-ratios.

While the present work focuses on the accuracy of various model formulations, the benchmarks could additionally be used to study effects of spatial discretization, time-stepping or other implementation details. This work was inspired by other efforts to connect the scientific community around phase-field modeling through benchmark problems [45–47] which have been collected on PFHub [48]. We try to cover the most common model formulations but are aware that the comparison is by no means complete. We hope the proposed benchmark serves the scientific community to collectively create a more complete picture and enhance future model developments.

Data availability

The source code to reproduce the simulations and post-processing can be obtained from the github repository `https://github.com/daubners/triple-junction-benchmark` [44].

Acknowledgments

References

[1] J. W. Cahn, J. E. Hilliard, Free Energy of a Nonuniform System. I. Interfacial Free Energy, The Journal of Chemical Physics 28 (2) (1958) 258–267. `doi:10.1063/1.1744102`.
URL `http://aip.scitation.org/doi/10.1063/1.1744102`

[2] J. W. Cahn, S. M. Allen, A Microscopic Theory for Domain Wall Motion and Its Experimental Verification in Fe-Al Alloy Domain Growth Kinetics, Le Journal de Physique Colloques 38 (December) (1977) C7–51. `doi:10.1051/jphyscol`.

[3] L.-Q. Chen, W. Yang, Computer simulation of the domain dynamics of a quenched system with a large number of nonconserved order parameters: The grain-growth kinetics, Physical Review B 50 (1994) 15752–15756. `doi:10.1103/PhysRevB.50.15752`.
URL `https://link.aps.org/doi/10.1103/PhysRevB.50.15752`

[4] N. Moelans, B. Blanpain, P. Wollants, An introduction to phase-field modeling of microstructure evolution, Calphad: Computer Coupling of Phase Diagrams and Thermochemistry 32 (2) (2008) 268–294. `doi:10.1016/j.calphad.2007.11.003`.

[5] I. Steinbach, F. Pezzolla, B. Nestler, M. Seeßelberg, R. Prieler, G. J. Schmitz, J. L. Rezende, A phase field concept for multiphase systems, Physica D: Nonlinear Phenomena 94 (3) (1996) 135–147. `doi:10.1016/0167-2789(95)00298-7`.

[6] B. Nestler, H. Garcke, B. Stinner, Multicomponent alloy solidification: Phase-field modeling and simulations, Physical Review E 71 (4) (2005) 041609. `doi:10.1103/PhysRevE.71.041609`.
URL `https://link.aps.org/doi/10.1103/PhysRevE.71.041609`

[7] J. D. van der Waals, Thermodynamische theorie der kapillarität unter voraussetzung stetiger dichteänderung, Zeitschrift für Physikalische Chemie 13U (1) (1894) 657–725 [cited 2022-07-08]. `doi:doi:10.1515/zpch-1894-1338`.
URL `https://doi.org/10.1515/zpch-1894-1338`

[8] V. L. Ginzburg, L. D. Landau, On the Theory of superconductivity, Zh.Eksp.Teor.Fiz. 20 (1950) 1064–1082.

[9] R. Kobayashi, Modeling and numerical simulations of dendritic crystal growth, Physica D: Nonlinear Phenomena 63 (3-4) (1993) 410–423. `doi:10.1016/0167-2789(93)90120-P`.
URL `https://linkinghub.elsevier.com/retrieve/pii/016727899390120P`

[10] J. Hötzer, M. Jainta, P. Steinmetz, B. Nestler, A. Dennstedt, A. Genau, M. Bauer, H. Köstler, U. Rüde, Large scale phase-field simulations of directional ternary eutectic solidification, Acta Materialia 93 (2015) 194–204. `doi:10.1016/j.actamat.2015.03.051`.
URL `https://linkinghub.elsevier.com/retrieve/pii/S135964541500227X`

[11] M. Kellner, J. Hötzer, E. Schoof, B. Nestler, Phase-field study of eutectic colony formation in NiAl-34Cr, Acta Materialia 182 (2020) 267–277. `doi:10.1016/j.actamat.2019.10.028`.

[12] H.-c. Yu, H.-y. Chen, K. Thornton, Extended smoothed boundary method for solving partial differential equations with general boundary conditions on complex boundaries, Modelling and Simulation in Materials Science and Engineering 20 (7) (2012) 075008. `doi:10.1088/0965-0393/20/7/075008`.
URL `https://iopscience.iop.org/article/10.1088/0965-0393/20/7/075008`

[13] D. A. Cogswell, M. Z. Bazant, Theory of Coherent Nucleation in Phase-Separating Nanoparticles, Nano Letters 13 (7) (2013) 3036–3041. `doi:10.1021/nl400497t`.
URL `https://pubs.acs.org/doi/10.1021/nl400497t`

[14] S. Daubner, M. Weichel, D. Schneider, B. Nestler, Modeling intercalation in cathode materials with phase-field methods: Assumptions and implications using the example of LiFePO4, Electrochimica Acta 421 (May) (2022) 140516. `doi:10.1016/j.electacta.2022.140516`.

[15] G. Gottstein, L. S. Shvindlerman, Grain Boundary Migration in Metals, 2nd Edition, Vol. 31, CRC Press, Boca Raton, Fla., 2009. `doi:10.1201/9781420054361`.

[16] I. Steinbach, F. Pezzolla, A generalized field method for multiphase transformations using interface fields, Physica D: Nonlinear Phenomena 134 (4) (1999) 385–393. `doi:10.1016/S0167-2789(99)00129-3`.
URL `https://linkinghub.elsevier.com/retrieve/pii/S0167278999001293`

[17] N. Moelans, B. Blanpain, P. Wollants, Quantitative analysis of grain boundary properties in a generalized phase field model for grain growth in anisotropic systems, Physical Review B - Condensed Matter and Materials Physics 78 (2) (2008). `doi:10.1103/PhysRevB.78.024113`.

[18] G. I. Tóth, T. Pusztai, L. Gránásy, Consistent multiphase-field theory for interface driven multidomain dynamics, Physical Review B 92 (18) (2015) 184105. `arXiv:1508.04311, doi:10.1103/PhysRevB.92.184105`.
URL `https://link.aps.org/doi/10.1103/PhysRevB.92.184105`

[19] A. Novick-Cohen, Triple-junction motion for an Allen–Cahn/Cahn–Hilliard system, Physica D: Nonlinear Phenomena 137 (1-2) (2000) 1–24. doi:10.1016/S0167-2789(99)00162-1.

[20] S. N. Enugala, Some refinements in the phase-field and sharp interface treatments of eutectic growth, Ph.D. thesis, Karlsruher Institut für Technologie (KIT), 38.04.04; LK 01 (2021). doi:10.5445/IR/1000134170.

[21] J. Eiken, B. Böttger, I. Steinbach, Multiphase-field approach for multicomponent alloys with extrapolation scheme for numerical application, Physical Review E 73 (6) (2006) 066122. doi:10.1103/PhysRevE.73.066122.

[22] I. Steinbach, Phase-field models in materials science, Modelling and Simulation in Materials Science and Engineering 17 (7) (2009) 073001. doi:10.1088/0965-0393/17/7/073001.
URL https://iopscience.iop.org/article/10.1088/0965-0393/17/7/073001

[23] N. Moelans, F. Wendler, B. Nestler, Comparative study of two phase-field models for grain growth, Computational Materials Science 46 (2) (2009) 479–490. doi:10.1016/j.commatsci.2009.03.037.
URL http://dx.doi.org/10.1016/j.commatsci.2009.03.037

[24] H. Garcke, B. Nestler, B. Stoth, A multiphase field concept: Numerical simulations of moving boundaries and multiple junctions, SIAM J. Appl. Math. 60 (1) (1999) 295–315.

[25] R. Folch, M. Plapp, Quantitative phase-field modeling of two-phase growth, Physical Review E 72 (1) (2005) 011602. doi:10.1103/PhysRevE.72.011602.
URL https://link.aps.org/doi/10.1103/PhysRevE.72.011602

[26] C. J. Grose, P. D. Asimow, A multi-phase field model for mesoscopic interface dynamics with large bulk driving forces, Computational Materials Science 212 (June) (2022) 111570. doi:10.1016/j.commatsci.2022.111570.

[27] E. Miyoshi, T. Takaki, M. Ohno, Y. Shibuta, Accuracy Evaluation of Phase-field Models for Grain Growth Simulation with Anisotropic Grain Boundary Properties, ISIJ International 60 (1) (2020) 160–167. doi:10.2355/isijinternational.ISIJINT-2019-305.

[28] W. W. Mullins, Two-dimensional motion of idealized grain boundaries, Journal of Applied Physics 27 (8) (1956) 900–904. doi:10.1063/1.1722511.

[29] J. Eiken, Discussion of the Accuracy of the Multi-Phase-Field Approach to Simulate Grain Growth with Anisotropic Grain Boundary Properties, ISIJ International 60 (8) (2020) 1832–1834. doi:10.2355/isijinternational.ISIJINT-2019-722.

[30] J. S. Langer, Models of Pattern Formation in First-Order Phase Transitions, in: Directions in Concensed Matter Physics: Memorial Volume in Honor of Shang-Keng Ma. Edited by GRINSTEIN S ET AL. Published by World Scientific Publishing Co. Pte. Ltd, 1986, pp. 165–186. doi:10.1142/9789814415309_0005.

[31] N. Provatas, K. Elder, Phase-Field Methods in Materials Science and Engineering, Wiley, 2010. doi:10.1002/9783527631520.
URL http://doi.wiley.com/10.1002/9783527631520

[32] Y. Wang, A. Khachaturyan, Three-dimensional field model and computer modeling of martensitic transformations, Acta Materialia 45 (2) (1997) 759–773. doi:10.1016/S1359-6454(96)00180-2.

[33] N. Moelans, A quantitative and thermodynamically consistent phase-field interpolation function for multi-phase systems, Acta Materialia 59 (3) (2011) 1077–1086. doi:10.1016/j.actamat.2010.10.038.
URL http://dx.doi.org/10.1016/j.actamat.2010.10.038

[34] O. Tschukin, A. Silberzahn, M. Selzer, P. G. Amos, D. Schneider, B. Nestler, Concepts of modeling surface energy anisotropy in phase-field approaches, Geothermal Energy 5 (1) (2017). doi:10.1186/s40517-017-0077-9.

[35] J. Tiaden, B. Nestler, H. Diepers, I. Steinbach, The multiphase-field model with an integrated concept for modelling solute diffusion, Physica D: Nonlinear Phenomena 115 (1-2) (1998) 73–86. doi:10.1016/S0167-2789(97)00226-1.
URL https://linkinghub.elsevier.com/retrieve/pii/S0167278997002261

[36] J. Hötzer, A. Reiter, H. Hierl, P. Steinmetz, M. Selzer, B. Nestler, The parallel multi-physics phase-field framework PACE3D, Journal of Computational Science 26 (2018) 1–12. doi:10.1016/j.jocs.2018.02.011.
URL https://doi.org/10.1016/j.jocs.2018.02.011

[37] L. D. Landau, E. M. Lifšic, Lehrbuch der theoretischen Physik, Band 5: Statistische Physik Teil 1, 8th Edition, Akademie-Verlag, Berlin, 1979.

[38] H. JÓNSSON, G. MILLS, K. W. JACOBSEN, Nudged elastic band method for finding minimum energy paths of transitions, in: Classical and Quantum Dynamics in Condensed Phase Simulations, WORLD SCIENTIFIC, 1998, pp. 385–404. doi:10.1142/9789812839664_0016.

[39] G. Henkelman, H. Jónsson, Improved tangent estimate in the nudged elastic band method for finding minimum energy paths and saddle points, The Journal of Chemical Physics 113 (22) (2000) 9978–9985. doi:10.1063/1.1323224.

[40] E. Schoof, D. Schneider, N. Streichhan, T. Mittnacht, M. Selzer, B. Nestler, Multiphase-field modeling of martensitic phase transformation in a dual-phase microstructure, International Journal of Solids and Structures 134 (2018) 181–194. doi:10.1016/j.ijsolstr.2017.10.032.
URL https://doi.org/10.1016/j.ijsolstr.2017.10.032

[41] S. Daubner, P. G. Kubendran Amos, E. Schoof, J. Santoki, D. Schneider, B. Nestler, Multiphase-field modeling of spinodal decomposition during intercalation in an Allen-Cahn framework, Physical Review Materials 5 (3) (2021) 035406. doi:10.1103/PhysRevMaterials.5.035406.
URL https://link.aps.org/doi/10.1103/PhysRevMaterials.5.035406

[42] J. Hötzer, O. Tschukin, M. B. Said, M. Berghoff, M. Jainta, G. Barthelemy, N. Smorchkov, D. Schneider, M. Selzer, B. Nestler, Calibration of a multi-phase field model with quantitative angle measurement, Journal of Materials Science 51 (4) (2016) 1788–1797. doi:10.1007/s10853-015-9542-7.
URL http://link.springer.com/10.1007/s10853-015-9542-7

[43] The PACE3D software package, https://www.iam.kit.edu/mms/english/5317.php, accessed: 2022-10-05.

[44] Github repository with code used for this publication:, `https://github.com/daubners/triple-junction-benchmark`.

[45] A. Jokisaari, P. Voorhees, J. Guyer, J. Warren, O. Heinonen, Benchmark problems for numerical implementations of phase field models, Computational Materials Science 126 (2017) 139–151. `doi:https://doi.org/10.1016/j.commatsci.2016.09.022`.
URL `https://www.sciencedirect.com/science/article/pii/S0927025616304712`

[46] A. Jokisaari, P. Voorhees, J. Guyer, J. Warren, O. Heinonen, Phase field benchmark problems for dendritic growth and linear elasticity, Computational Materials Science 149 (2018) 336–347. `doi:https://doi.org/10.1016/j.commatsci.2018.03.015`.
URL `https://www.sciencedirect.com/science/article/pii/S092702561830168X`

[47] W. Wu, D. Montiel, J. Guyer, P. Voorhees, J. Warren, D. Wheeler, L. Gránásy, T. Pusztai, O. Heinonen, Phase field benchmark problems for nucleation, Computational Materials Science 193 (2021) 110371. `doi:https://doi.org/10.1016/j.commatsci.2021.110371`.
URL `https://www.sciencedirect.com/science/article/pii/S0927025621000963`

[48] PFHub: The Phase Field Community Hub, `https://pages.nist.gov/pfhub/`, accessed: 2022-08-01.

[49] A. Reiter, Some Impliciations of Constraints in Phasefield Models, Phd thesis, Karlsruhe Institute of Technology (KIT) (2020).

Appendix A. Two-phase interphase

Appendix A.1. Energy functional

We start from a functional defined in terms of one order parameter, assuming spatial isotropy

$$\mathcal{F}(\phi, \boldsymbol{\nabla}\phi) = \int_V \kappa|\boldsymbol{\nabla}\phi|^2 + f_{\text{pot}}(\phi)\mathrm{d}V.$$

The potential energy is typically formulated in terms of a double-well or double obstacle function where the parameter Ω scales the energetic barrier to be overcome

$$f_{\text{well}}(\phi) = \Omega\phi^2(1-\phi)^2$$
$$f_{\text{ob}}(\phi) = \Omega\phi(1-\phi) \quad \forall \phi \in [0,1] \text{ and } \infty \text{ otherwise.}$$

The evolution equation for ϕ is given under the assumption of energy minimization with linear kinetics

$$\dot{\phi} = -L\left(\frac{\partial}{\partial\phi} - \boldsymbol{\nabla}\cdot\frac{\partial}{\partial\boldsymbol{\nabla}\phi}\right)(f_{\text{grad}} + f_{\text{pot}})$$

which finally leads to

$$\dot{\phi} = -L\left[-2\kappa\boldsymbol{\nabla}^2\phi + \frac{\partial f_{\text{pot}}}{\partial\phi}\right] \quad \text{where } \frac{\partial f_{\text{pot}}}{\partial\phi} = \begin{cases} \text{well:} & 2\Omega\phi(1-2\phi)(1-\phi) \\ \text{obstacle:} & \Omega(1-2\phi) \end{cases} \tag{A.1}$$

Appendix A.2. Interfacial properties

Following the procedure in Cahn and Hilliard [1], we can derive the interfacial properties of the diffuse interface. The equilibrium solution is given by $\dot{\phi} = 0$ which yields for a 1D flat interface

$$2\kappa\boldsymbol{\nabla}^2\phi = \frac{\partial f_{\text{pot}}}{\partial\phi} \quad \rightarrow \kappa\left(\frac{\partial\phi}{\partial x}\right)^2 = f_{\text{pot}} \quad \rightarrow \mathrm{d}x = \sqrt{\kappa/f_{\text{pot}}}\mathrm{d}\phi.$$

The surface energy of a flat interface is given by the excess Gibbs free energy across the diffuse region

$$\gamma = \int_{-\infty}^{\infty} \kappa(\boldsymbol{\nabla}\phi)^2 + f_{\text{pot}}\mathrm{d}x = 2\int_{-\infty}^{\infty} f_{\text{pot}}\mathrm{d}x = 2\int_0^1 \sqrt{\kappa f_{\text{pot}}}\mathrm{d}\phi = \sqrt{\kappa\Omega}\begin{cases} 1/3 & \text{(well)} \\ \pi/4 & \text{(obstacle)} \end{cases} \tag{A.2}$$

While the obstacle potential leads to a sinus profile which has a finite interfacial width, the well potential leads to a tanh function. For both cases the interfacial width can be defined by the linear tangent fit in $\phi = 0.5$ such that

$$l_{\text{int}} = \frac{1}{\mathrm{d}\phi/\mathrm{d}x}\Big|_{\phi=0.5} = \sqrt{\frac{\kappa}{f_{\text{pot}}(\phi=0.5)}} = \sqrt{\frac{\kappa}{\Omega}}\begin{cases} 4 & \text{(well)} \\ 2 & \text{(obstacle)} \end{cases} \tag{A.3}$$

Appendix B. Functional derivatives

Appendix B.1. Gradient term

Table B.4: Common gradient energy formulations and their variation with respect to ϕ_α

f_{grad}	$\delta f_{\text{grad}}/\delta\phi_\alpha$
$\frac{1}{2}\sum_\alpha \kappa_\alpha|\boldsymbol{\nabla}\phi_\alpha|^2$	$-\kappa_\alpha\boldsymbol{\nabla}^2\phi_\alpha$
$\frac{1}{2}\frac{\sum\sum\kappa_{\alpha\beta}\phi_\alpha^2\phi_\beta^2}{\sum\sum\phi_\alpha^2\phi_\beta^2}\sum_\alpha|\boldsymbol{\nabla}\phi_\alpha|^2$	$\frac{1}{2}\frac{\partial\tilde{\kappa}}{\partial\phi_\alpha}\sum_\alpha|\boldsymbol{\nabla}\phi_\alpha|^2 - \boldsymbol{\nabla}\cdot(\tilde{\kappa}\boldsymbol{\nabla}\phi_\alpha)$
$\sum_\alpha\sum_{\beta>\alpha}\kappa_{\alpha\beta}|\phi_\alpha\boldsymbol{\nabla}\phi_\beta - \phi_\beta\boldsymbol{\nabla}\phi_\alpha|^2$	$\sum_{\beta\neq\alpha}2\kappa_{\alpha\beta}\left(2\phi_\alpha|\boldsymbol{\nabla}\phi_\beta|^2 - 2\phi_\beta\boldsymbol{\nabla}\phi_\alpha\cdot\boldsymbol{\nabla}\phi_\beta + \phi_\alpha\phi_\beta\boldsymbol{\nabla}^2\phi_\beta - \phi_\beta^2\boldsymbol{\nabla}^2\phi_\alpha\right)$
$-\sum_\alpha\sum_{\beta>\alpha}\kappa_{\alpha\beta}\boldsymbol{\nabla}\phi_\alpha\cdot\boldsymbol{\nabla}\phi_\beta$	$\sum_{\beta\neq\alpha}\kappa_{\alpha\beta}\boldsymbol{\nabla}^2\phi_\beta$

Appendix B.2. Potential term

Table B.5: Common potential term formulations and their variation with respect to ϕ_α

f_{pot}	$\delta f_{\text{pot}}/\delta\phi_\alpha$
$\frac{1}{2}\sum_\alpha\sum_{\beta>\alpha}\Omega_{\alpha\beta}\phi_\alpha^2\phi_\beta^2 + \tilde{\Omega}\Big(\frac{1}{12} + \sum_\alpha\Big(\frac{\phi_\alpha^4}{4} - \frac{\phi_\alpha^3}{3}\Big)\Big)$	$\phi_\alpha\sum_{\beta\neq\alpha}\Omega_{\alpha\beta}\phi_\beta^2 + \tilde{\Omega}(\phi_\alpha^3 - \phi_\alpha^2) + \frac{\partial\tilde{\Omega}}{\partial\phi_\alpha}\big(\frac{1}{12} + \dots\big)$
$\frac{3}{4}\sum_\alpha\sum_{\beta>\alpha}\Omega_{\alpha\beta}\phi_\alpha^2\phi_\beta^2 + \frac{1}{2}\tilde{\Omega}\Big(\frac{1}{4} + \sum_\alpha\Big(\frac{\phi_\alpha^4}{4} - \frac{\phi_\alpha^2}{2}\Big)\Big)$	$\frac{3}{2}\phi_\alpha\sum_{\beta\neq\alpha}\Omega_{\alpha\beta}\phi_\beta^2 + \frac{1}{2}\tilde{\Omega}(\phi_\alpha^3 - \phi_\alpha) + \frac{1}{2}\frac{\partial\tilde{\Omega}}{\partial\phi_\alpha}\big(\frac{1}{4} + \dots\big)$
$\sum_\alpha\sum_{\beta>\alpha}\Omega_{\alpha\beta}\phi_\alpha^2\phi_\beta^2 + \sum_\alpha\sum_{\beta>\alpha}\sum_{\gamma>\beta}\Omega_{\alpha\beta\gamma}\phi_\alpha^2\phi_\beta^2\phi_\gamma^2$	$2\phi_\alpha\sum_{\beta\neq\alpha}\Omega_{\alpha\beta}\phi_\beta^2 + 2\phi_\alpha\sum_{\beta\neq\alpha}\sum_{\gamma>\beta}\Omega_{\alpha\beta\gamma}\phi_\beta^2\phi_\gamma^2$
$\sum_\alpha\sum_{\beta>\alpha}\Omega_{\alpha\beta}\phi_\alpha\phi_\beta$	$\sum_{\beta\neq\alpha}\Omega_{\alpha\beta}\phi_\beta$

Appendix C. Model notations

Table C.6: Comparison of notations used in different publications and in this paper.

parameter	multi-order parameter		multi-phase field			this
	Chen *et al.* [3]	Moelans *et al.* [17]	Eiken *et al.* [21]	Nestler *et al.* [6]	Toth *et al.* [18]	work
gradient energy coeff. (J/m)	κ_i	$\kappa_{i,j}$	$4\sigma_{\alpha\beta}\eta_{\alpha\beta}/\pi^2$	$\varepsilon\gamma_{\alpha\beta}$	$3\delta_{ij}\gamma_{ij}$	$\kappa_{\alpha\beta}$
multi-well parameter(s) (J/m^3)	α,β,γ	$m,\gamma_{i,j}$	-	$9\gamma_{\alpha\beta}/\varepsilon$	$3\gamma_{ij}/\delta_{ij}$	$\Omega_{\alpha\beta},\chi$
multi-obstacle barrier (J/m^3)	-	-	$4\sigma_{\alpha\beta}/\eta_{\alpha\beta}$	$16\gamma_{\alpha\beta}/\varepsilon\pi^2$	-	$\Omega_{\alpha\beta}$
kinetic coefficient (m^3/Js)	L_i	$L_{i,j}$	$M_{\alpha\beta}/\varepsilon$	$1/\tau\varepsilon$	κ_{ij}	$L_{\alpha\beta}$
interface energy (J/m^2)	-	$\sigma_{i,j}$	$\sigma_{\alpha\beta}$	$\gamma_{\alpha\beta}$	γ_{ij}	$\gamma_{\alpha\beta}$
interface width (m)	-	l_{gb}	$2\eta_{\alpha\beta}/\pi$	$\varepsilon\pi/2$	δ_{ij}	Eq. (A.3)

Appendix D. Gibbs simplex constraint

In multiphase-field models, the phase-field variable ϕ_α corresponds to the volume fraction of the respective phase which makes it necessary to fulfill the Gibbs simplex constraint

$$\boldsymbol{\phi}\in\mathbb{R}^N:\sum_{\alpha=1}^N\phi_\alpha = 1,\quad 0\leq\phi_\alpha\quad\forall\alpha. \tag{D.1}$$

If the sum constraint is fulfilled and all phases fractions are larger than zero, we implicitly ensure $\phi_\alpha\in[0,1]$ $\forall\alpha=1,\dots,N$. Given that the initial conditions comply with Eq. (D.1), there are two conditions that need to be fulfilled during the evolution of phase-field variables, namely

$$\sum_\alpha\frac{\partial\phi_\alpha}{\partial t} = 0\quad\text{and}\quad 0\leq\phi_\alpha\quad\forall\alpha.$$

The first conditions is ensured by correct formulation of the evolution equations, either by introducing a Langrange multiplier (see Eq. (19)) or by suitable choice of the mobility matrix which results in the sum over dual-interactions in Eq. (20). If the choice of energy contributions can lead to nonphysical values of $\phi_\alpha<0$, this violation of constraint Eq. (D.1) needs to be handled separately. Depending on the discretization of time stepping, there are two possible options

1. **Projection-based approach:** We separate the total problem into two a priori simpler problems where the first one is computation of the evolution equations (e.g. $\phi_\alpha^{\text{new}} = \phi_\alpha^{\text{old}} + \Delta t(\dots)$) neglecting the additional constraints and thus violation of $\phi_\alpha \in [0,1]$ might occur. In a subsequent step, the tuple of phase variables ϕ is projected back onto the admissible set (sort of "pushed back into the Gibbs triangle"). Differences in pairwise mobilities must be taken into account for this procedure to ensure correct treatment of the underlying physics.

2. **Holistic approach:** The condition $0 \leq \phi_\alpha$ enters the system of equations as an algebraic constraint. For large numbers of phases N the problem growths disproportionally with $\propto N^2$ as for every cell/ grid point $N-1$ evolution equations plus N algebraic constraints must be computed.

While the projection method can be implemented in a fully explicit and local manner (i.e. cell-wise computation of the prediction ϕ_*^{new} and projection ϕ^{new}), the holistic approach needs global convergence of ϕ-values and all interdependend physical fields (e.g. concentration c).

Projection into the Gibbs triangle

For the binary case of $\phi_\alpha = \phi$ and $\phi_\beta = 1 - \phi$, it is sufficient to check for the criterion $\phi < 0$ and, if fulfilled, set $\phi = 0$. Similarly, values of $\phi > 1$ are pushed back to $\phi = 1$. This results in one line of (pseudo-)code

$$\phi^{\text{new}} = \max(0, \min(\phi^{\text{new}}, 1)). \tag{D.2}$$

For the general case of N phases, the procedure is more complicated and will be illustrated over the Gibbs simplex of a triple junction. A detailed discussion of various projection methods can be found in [49]. Far enough from the triple junction (where 'far enough' depends on the width of the diffuse interface), the three-phase system should reduce to a binary interface or bulk ($\phi_\alpha = 1$). Assuming $\phi_\gamma = 0$, any change of phase-variables occurs along the $\alpha\beta$-side of the triangle highlighted in green in Fig. D.11b. A violation of Eq. (18), e.g. $\phi_\alpha < 0$ (and thus $\phi_\beta > 1$) as sketched by circle 1, can essentially be handled by Eq. (D.2) and the projection along the green arrow yields $\phi_\alpha = 0$ and $\phi_\beta = 1$. The second scenario is well within the
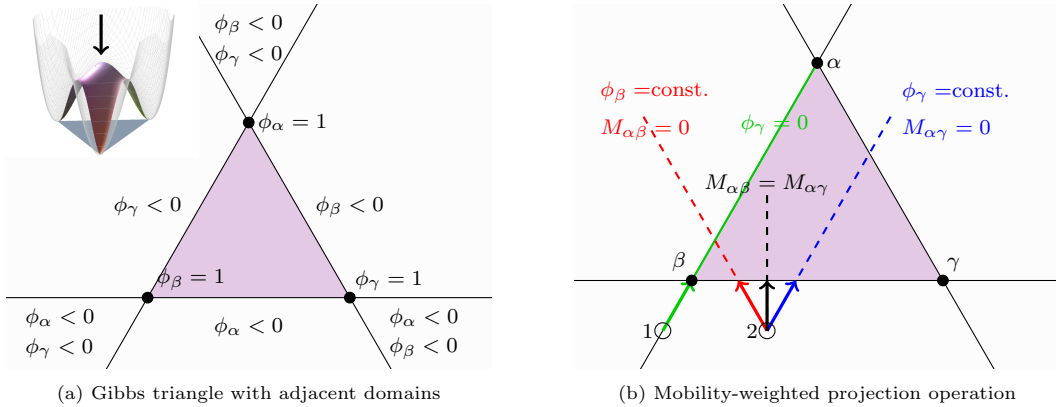

(a) Gibbs triangle with adjacent domains

(b) Mobility-weighted projection operation

Figure D.11: Visualization of the Gibbs simplex for a triple junction as the purple triangle while domains fullfilling the sum constraint but violating the positivity constraint $\phi_\alpha \leq 0$ are shown in light gray. The sketch can be interpeted as the top-view onto the energy landscape as shown in a). The mobility-weighted projection into the Gibbs simplex is shown in b) for the case of a binary interface (1) and a general three-phase case (2).

triple junction and again we assume violation of positivity by $\phi_\alpha < 0$. The projection back into the Gibbs triangle now depends on the ratio of pairwise mobilities. In Fig. D.11b, the two limiting cases of $M_{\alpha\beta} = 0$ and $M_{\alpha\gamma} = 0$ are shown together with the case of equal mobilities. The projection algorithm is constructed such that the phase with a negative value will be set to zero $\phi_\alpha = 0$. Incorporation of mobilities is crucial to avoid nonphysically fast evolution of 'slow' phases. Assume that ϕ_γ is a highly immobile phase, any violation of Eq. (18) occurs along the blue dashed direction. A projection performed without consideration

of mobility ratios results in the operation sketched with a black arrow and would, thus, allow ϕ_γ to zig-zag its way along the lower side of the triangle, resulting in faster kinetics accelerated by the Gibbs simplex algorithm. The general N-dimensional procedure is sketched in the following pseudo-code

---

Algorithm 1: Gibbs simplex implementation for N phases

---

for $\alpha = 1 \ldots N$ **do**
    if $\phi_\alpha < 0$ **then**
        activateGibbsSimplex[α] = true;
        count_violations++;

if (count_violations==0) **then** return;   all phases fulfill $\phi_\alpha \in [0,1]$

done=false;
M_{red}=zeros[N,N]; $M_{\mathrm{red}} \in \mathbb{R}^{N \times N}$: reduction of $M_{\alpha\beta}$ to phases violating $\phi_\alpha \leq 0$.
b=zeros[N];
while *not done* **do**
    for $\alpha = 1 \ldots N$ **do**
        if (!activateGibbsSimplex[α]) **then** continue;
        b[α]=$-\phi_\alpha$;
        $M_{\mathrm{red}}[\alpha, \alpha] = M_{\alpha\alpha}$;
        for $\beta = \alpha + 1 \ldots N$ **do**
            if (!activateGibbsSimplex[β]) **then** continue;
            $M_{\mathrm{red}}[\alpha, \beta] = M_{\alpha\beta}$;
            $M_{\mathrm{red}}[\beta, \alpha] = M_{\alpha\beta}$;
    solve($M_{\mathrm{red}}\boldsymbol{x} = \boldsymbol{b}$ for $\boldsymbol{x}$);   any vecor-matrix solving algorithm, e.g. Gauss elimination.
    done=true;

    for $\alpha = 1 \ldots N$ **do**
        $\phi_\alpha^{\mathrm{new}} = \phi_\alpha^{\mathrm{new}} + M_{\alpha\beta}x_\beta$
        if ($\phi_\alpha^{\mathrm{new}} < 0$) **then** done=false;

Appendix E. Analytic details for GB in steady state motion

Appendix E.1. Solving the geometry ODE

The grain boundary geometry can be described by the ordinary differential equation

$$y''(x) = -\frac{V}{M_0\gamma_0}\left(1 + (y'(x))^2\right). \tag{E.1}$$

To simplify the analysis, we introduce the following dimensionless quantities $u \equiv \frac{x}{W}$, $z \equiv \frac{y}{W}$ and $v \equiv (VW)/(M_0\gamma_0)$. It follows, that $y'(x) = z'(u)$ and $y''(x) = z''(u)/W$ and, hence, we obtain

$$z''(u) = -v\left(1 + (z'(u))^2\right). \tag{E.2}$$

The boundary conditions remain unchanged such that $z(\pm 1/2) = 0$ and $z'(\pm 1/2) = \mp m$ hold. Eq. (E.2) is a nonlinear first order differential equation for z' which can be solved by separation and integration. The dimensionless steady-state velocity is obtained as a function of the triple-junction slope m

$$v = 2\arctan(m), \tag{E.3}$$

i.e. in dimensional form

$$V = \frac{2M_0\gamma_0}{W}\arctan(m). \tag{E.4}$$

27

The non-dimensional solution of the grain boundary geometry is

$$z(u) = \frac{\ln\left(\cos\left(2\arctan(m)u\right)\right) - \ln\left(\cos\left(\arctan(m)\right)\right)}{2\arctan(m)}, \tag{E.5}$$

which can be expressed in terms of θ as

$$z(u) = \frac{\ln\left(\cos\left((\pi-\theta)u\right)\right) - \ln\left(\sin\left(\theta/2\right)\right)}{\pi-\theta}. \tag{E.6}$$

Re-expressing this solution with physical quantities results in Eq. (41). The aspect ratio of the GB, $h_{\mathrm{GB}}/W = y(0)/W$ is related to the dihedral angle by

$$\frac{h_{\mathrm{GB}}}{W} = \frac{\ln\left(\sin\left(\theta/2\right)\right)}{\theta-\pi}. \tag{E.7}$$

By inverting the above equation, θ can be determined as a function of the aspect ratio given that h_{GB}/W is known. A good approximation for the inversion is given by

$$\theta\left(\frac{h_{\mathrm{GB}}}{W}\right) \approx \theta_0 = \left(\frac{7}{5}\exp\left(-\frac{h_{\mathrm{GB}}}{W}\right)\right)^{\frac{7}{2}}. \tag{E.8}$$

Refinements are done using Newton iterations $\theta_{i+1} = \theta_i + \Delta\theta_i$ where the update per step is defined as

$$\Delta\theta_i = \frac{\exp\left(-\frac{h_{\mathrm{GB}}}{W}\right)\sin^{\frac{1}{\theta_i-\pi}}\left(\frac{\theta_i}{2}\right)-1}{\frac{\pi-\theta_i}{2}\cot\left(\frac{\theta_i}{2}\right)+\ln\left(\sin\left(\frac{\theta_i}{2}\right)\right)}(\pi-\theta_i)^2. \tag{E.9}$$

The Newton procedure converges rapidly within four iterations with an estimated error of $|\Delta\theta_4| < 10^{-12}$. We use this procedure to determine the resulting dihedral angle from simulation results.

Appendix E.2. Small-slope Approximation

The assumption $|y'| << 1$ leads to $V \approx v_n$ which is a small-slope approximation (SSA) of the problem described in Sec. 3.2. Anticipating that $|y'|$ is on the order of m leads to $m << 1$. Within the SSA, the curvature is a constant $\kappa = 1/R$ and the grain boundary geometry is described by the circular arc

$$y(x) = \sqrt{R^2 - x^2} + y_m \tag{E.10}$$

with radius R and midpoint y-coordinate y_m. From the Dirichlet BCs, we derive $y_m = -\frac{W}{2}\tan(\theta/2)$. Compliance with the Neumann conditions stated above, yields a relation for the curvature in the small-slope approximation

$$R = \frac{W}{2}\frac{\sqrt{1+m^2}}{m}. \tag{E.11}$$

Accordingly, the interface velocity can be written in terms of the slope m

$$V = M_0\gamma_0\frac{2m}{W\sqrt{1+m^2}} \approx M_0\gamma_0\frac{2m}{W} \tag{E.12}$$

where the approximation is based on $m << 1$. By exploiting $m = \cot(\theta/2)$, R and the velocity V can be expressed in terms of the angle θ

$$R = \frac{W}{2}\frac{1}{\cos(\theta/2)} \quad \text{and} \quad V = M_0\gamma_0\frac{2\cos(\theta/2)}{W}. \tag{E.13}$$

This relation was used in [23] (Eq. (33)) while the limitation to small slopes has not been not mentioned.